Mass-transfer driven spinodal decomposition in a ternary polymer solution

Douglas R. Tree,[†] Lucas F. Dos Santos ,[‡] Caden B. Wilson,[†] Timothy R. Scott,[†] Jan Ulric Garcia,[¶] and Glenn H. Fredrickson[*,§,‖,¶]

[†]*Chemical Engineering Department, Brigham Young University, Provo, Utah*
[‡]*State University of Maringá, Maringá, Paraná, Brazil*
[¶]*Chemical Engineering Department, University of California, Santa Barbara*
[§]*Materials Research Laboratory, University of California, Santa Barbara*
[‖]*Materials Department, University of California, Santa Barbara*

E-mail: tree.doug@byu.edu

Abstract

Nonsolvent induced phase separation (NIPS) is a widely occuring process used in industrial membrane production, nanotechnology and Nature to produce microstructured polymer materials. A variety of process-dependent morphologies are produced when a polymer solution is exposed to a nonsolvent that, following a period where mass is exchanged, precipitates and solidifies the polymer. Despite years of investigation, both experimental and theoretical, many questions surround the pathways to the microstructures that NIPS can produce. Here, we provide simulation results from a model that simultaneously captures both the processess of solvent/nonsolvent exchange and phase separation. We show that the time it takes the nonsolvent to diffuse to the bottom of the film is an important timescale, and that phase separation is possible at times both much smaller and much larger than this scale. Our results include both one-dimensional simulations of the mass transfer kinetics and two- and three-dimensional simulations of morphologies at both short and long times. We find good qualitative agreement with experimental heuristics, but we conclude that an additional model for the vitrification process will be key for fully explaining experimental observations of microstructure formation.

Introduction

Non-solvent induced phase separation (NIPS) is a process where a polymer solution is driven into a two-phase region by exchanging a good solvent for a poor one and is widely used in industry,[1] nanotechnology[2,3] and biological systems[4] for generating micro-structured polymer materials. In this manuscript we consider the industrially relevant example of a polymer membrane made by immersion precipitation as a proxy for the generic NIPS process. As shown in Figure 1, immersion precipitation membranes are made by coating a polymer solution onto a flat substrate, followed by immersion into a non-solvent bath. After sufficient exchange of solvent and non-solvent, the film separates into polymer-rich and polymer-lean phases. Eventually, the increasing polymer concentration of the polymer-rich phase causes the microstructure of the film to arrest in a non-equilibrium state, forming the membrane.

Despite its prevalence, there are many details of immersion precipitation that are not well understood, including the fundamental kinetics of the mass-transfer initiated phase separation process. The community's lack of understanding is not a result of negligence; in the late 1980's and early 1990's several researchers developed one-dimensional mass-transport mod-

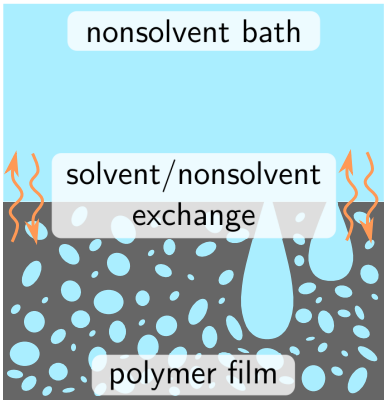

Figure 1: Schematic of the immersion precipitation process, where nonsolvent/solvent exchange drives a phase separation in a polymer film.

els of solvent and non-solvent diffusion for immersion precipitation membranes.[5–7] However, such models did not include phase separation kinetics—a critical omission—leaving all predictions of the resulting phase separation to be inferred from single phase concentration profiles.

While largely ignored by these early transport models, the isolated study of the phase separation kinetics of polymer solutions have also been a frequent topic in the literature.[8–10] Here, in contrast to the immersion precipitation process, the lion's share of attention for these studies has been on phase separation in a binary, isotropic system following a temperature quench. Work on anisotropic systems includes research on temperature-driven surface-directed spinodal decomposition where symmetry is broken by the surface.[11,12] Additionally, several groups (including us) have recently studied an initially inhomogeneous ternary polymer solution undergoing spinodal decomposition initiated by a temperature quench.[13–16] In both of the latter studies, mass transfer between the bath and film phases was present, but solvent/non-solvent exchange did not initiate the phase separation.

Thus while both solvent/non-solvent exchange and phase separation kinetics of the NIPS process in a ternary polymer solution have been previously studied, researchers have examined them as separate phenomena. However, the intimate coupling between mass transfer and phase separation is a hallmark of the NIPS process, since solvent/non-solvent exchange drives the phase separation. As such, determining how solvent/non-solvent exchange initiates and affects the kinetics of phase separation is critical to understanding NIPS, and remains an important open question.

One of the principal challenges to understanding the NIPS process has been the lack of robust models capable of reaching the relevant length and time scales. In a recent paper,[15] we addressed this challenge by deriving and validating a model using the two-fluid formalism of de Gennes, Doi and Onuki.[17,18] Along with the model, we developed an efficient pseudo-spectral method that permits large-scale, long-time simulations of mass transport and phase separation dynamics.

Even with our method, the need to resolve a large non-solvent reservoir presents an additional computational hurdle to modeling solvent/non-solvent exchange in the NIPS process. The most computationally efficient way to handle the reservoir is to use time-dependent, non-homogeneous boundary conditions, which are difficult to incorporate into a pseudo-spectral method. To overcome this limitation, we have developed a hybrid finite-difference/pseudo-spectral (FD/PS) method to generalize the types of boundary conditions that can be imposed.

With this tool in hand, we use our previously developed multi-fluid model[15] to study the simultaneous processes of solvent/non-solvent exchange and spinodal decomposition in an immersion precipitation-like geometry. We first review our model and outline the FD/PS method, and we also provide a brief review of several existing theories that are key to understanding our results. We then discuss two different regimes of behavior: (i) phase separations that occur on times much less than the diffusion time of the nonsolvent and (ii) phase separations that occur on much larger timescales. In both regimes, we examine how the initial concentration of polymer and nonsolvent in the film influences the phase separation kinetics and the morphology. Finally, we con-

clude with a discussion of the relevance of this work for membrane formation.

Model and Methods

To simulate the NIPS process, we use a multi-fluid model of a ternary polymer solution, which was derived and characterized in a previous publication.[15] The model consists of diffusion equations for the independent polymer (p) and non-solvent (n) components, a (vector) momentum equation and an incompressibility constraint,

$$\frac{\partial \phi_i}{\partial t} + \boldsymbol{v} \cdot \nabla \phi_i = \nabla \cdot \left[\sum_j^{p,n} M_{ij} \nabla \mu_j \right] \quad (1)$$

$$0 = -\nabla p + \nabla \cdot \left[\eta (\nabla \boldsymbol{v} + \nabla \boldsymbol{v}^T) \right] - \nabla \cdot \boldsymbol{\Pi} \quad (2)$$

$$\nabla \cdot \boldsymbol{v} = 0. \quad (3)$$

In these equations $\boldsymbol{v}$ is the volume averaged velocity, ϕ_i is the volume fraction of species i, M_{ij} is the mobility matrix, μ_i is the chemical potential of species i, p is the pressure, η is the solution viscosity and $\boldsymbol{\Pi}$ is the osmotic stress. Because of incompressibility, the solvent (s) volume fraction is not an independent quantity and is completely determined by

$$\phi_s = 1 - \phi_p - \phi_n. \quad (4)$$

Notably, Equations 1–3 do not contain noise terms and thus neglect thermal fluctuations. This simplifying assumption makes it impossible to observe barrier-crossing phenomena such as nucleation with the present model.

The chemical potential in Eq. 1 is given by,

$$\mu_i = \frac{k_B T}{\mathrm{v}_0} \left(\frac{\partial f_0}{\partial \phi_i} - \kappa_i \nabla^2 \phi_i \right) \quad (5)$$

where

$$f_0(\{\phi_i\}) = \sum_i^{p,n,s} \frac{\phi_i}{N_i} \ln \phi_i + \frac{1}{2} \sum_{i \neq j}^{p,n,s} \chi_{ij} \phi_i \phi_j \quad (6)$$

is the Flory–Huggins free energy density of a homogeneous polymer solution, v_0 is the monomer volume, k_B is Boltzmann's constant, T is the absolute temperature and κ_i are gradient coefficients. The homogeneous free energy, f_0, contains parameters characterizing the molecular weight of the components, N_i, and the pairwise interactions between species, χ_{ij}. The mobility coefficients appearing in Eq. 1 are defined as,

$$M_{pp} = \frac{\mathrm{v}_0}{\zeta_0} \phi_p (1 - \phi_p) \quad (7a)$$

$$M_{pn} = M_{np} = -\frac{\mathrm{v}_0}{\zeta_0} \phi_p \phi_n \quad (7b)$$

$$M_{nn} = \frac{\mathrm{v}_0}{\zeta_0} \phi_n (1 - \phi_n) \quad (7c)$$

where $\zeta_0 = \eta_s b$ is the monomer friction coefficient with η_s the solvent viscosity and b the monomer size.

The osmotic stress tensor in Eq. 2 describes the forces driving chemical diffusion and is completely determined by the chemical potential.[18,19] Its divergence is given by[15]

$$\nabla \cdot \boldsymbol{\Pi} = \phi_n \nabla \mu_n + \phi_p \nabla \mu_p. \quad (8)$$

Additionally, the volume-fraction dependent viscosity in Eq. 2 is assumed to be consistent with a Rouse model of polymer solutions,

$$\eta = \eta_s (1 + c \phi_p N_p) \quad (9)$$

where c is a constant that is set to unity, unless otherwise noted.

The multi-fluid model is solved numerically on CPUs and GPUs using a custom-written CUDA/C++ program.[15] Time is discretized with a simple Euler scheme where linear terms are treated implicitly, providing needed stability to small-scale modes. The semi-implicit Euler scheme is complemented with a variable time-stepping procedure, which dramatically decreases the total run-time by accelerating/decelerating the simulation during periods of slower/faster dynamics. Space is discretized using either a pseudo-spectral method or a hybrid finite-difference/pseudo-spectral method as described below.

The NIPS process requires an initial geometry with two regions: a non-solvent bath and a polymer film, as shown in Figure 2. The initial composition of the film consists of a mixture

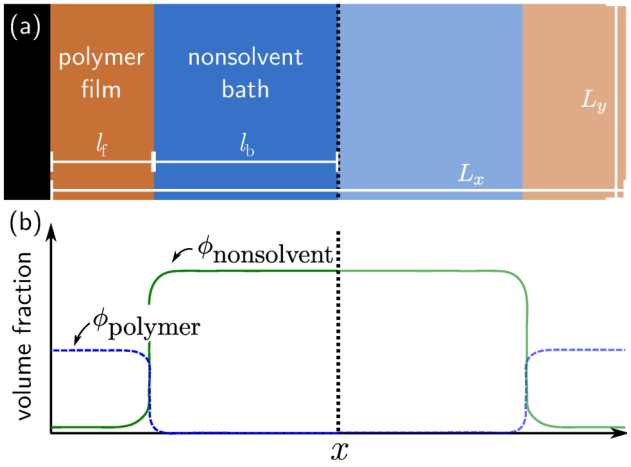

Figure 2: (a) A 2D representation of the simulation geometry for a polymer film of thickness l_f and bath height l_b. With periodic boundary conditions, one employs an initial condition that is symmetric about the dashed center-line and $l_b \gg l_f$. For non-periodic boundary conditions where the bath composition is known, no such requirements are necessary, but different methods must be used to discretize space. (b) A 1D plot showing example polymer and non-solvent volume fractions in both film and bath domains corresponding to the 2D schematic in panel (a).

of polymer, solvent and possibly non-solvent, and the initial bath concentration is pure non-solvent. The bottom of the film is impermeable, giving a no-flux condition at the film/substrate interface. The bath is infinite, which is computationally realized by making the size of the bath l_b much larger than the film size, l_f.

We use two different approaches to model the system geometry given in Figure 2. For one-dimensional simulations we assume that the system is periodic, and use symmetry to enforce a no-flux boundary condition at $x = 0$ and $x = L_x/2$. The principle advantage of this setup is the straightforward use of pseudo-spectral methods to treat spatial derivatives, which are both simple to program and offer unparalleled accuracy for resolving the narrow interfaces between phases. The downside of using pseudo-spectral methods and periodic boundary conditions is the required size of the non-solvent bath, l_b, which must be very large to reach the "infinite bath" limit. Resolving such a large domain wastes valuable computational resources on a mostly homogeneous bath. In fact, even with our optimized method, these costs become prohibitively expensive for long simulations as the diffusive boundary layer grows without bound as time proceeds. Because of these costs, simulations with an explicit bath are generally limited to one-dimension (1D)—a severe constraint indeed.

To avoid this problem, our second approach is to use explicit boundary conditions at both the film/substrate interface and near the film/bath interface. Because non-homogeneous boundary conditions are difficult to implement in a purely pseudo-spectral algorithm, we use a hybrid pseudo-spectral/finite difference (PS/FD) method for the spatial derivatives that more readily accommodates complicated boundary conditions. The hybrid scheme, which is described in detail in the Supplemental Information, discretizes spatial derivatives in one dimension (e.g. x) by finite differences, and the remaining dimensions (e.g. y and z) pseudo-spectrally. The dimension discretized by finite differences acquires the flexibility to represent time-dependent, non-homogeneous boundary conditions, while the other dimensions retain the accuracy properties and efficiency inherent to PS methods. Additionally, since only one dimension is represented by FD, the numerical method retains its nearly ideal $O(\mathcal{M} \log \mathcal{M})$ scaling where $\mathcal{M}$ is the total number of points in the collocation and finite difference grids.

With this additional capability, we are able to simulate the NIPS process in 2D and 3D. Practically, this is accomplished by first running a 1D simulation with $l_b \gg l_f$ to calculate the time-dependent concentration profile of the bath. In a subsequent multi-dimensional simulation, the length of the bath is truncated and time-varying species concentrations and first derivatives obtained from the 1D simulation are prescribed at the bath interface and the wall. (Note that when hydrodynamics are included, the size of the new bath must still be large enough to account for near-interface velocities in the bath.)

Summary of Theory

Before discussing the results of our simulation study, it is necessary to provide some context by summarizing a few relevant theories. To simplify Equations 1–3 for analysis, we assume a one-dimensional geometry, pseudo-binary parameters: $\chi_{ps} = \chi_{ns} = 0$, $N_n = N_s = 1$, $N_p = N$ and equal gradient coefficients $\kappa = \kappa_p = \kappa_n$. By simplifying to one dimension we also implicitly assume quiescent conditions (i.e. $\boldsymbol{v} = 0$), eliminating the momentum and incompressibility equations. Using these assumptions, we substitute the chemical potential from Eq. 5 into the diffusion equation in Eq. 1 and use the chain rule to obtain,

$$\frac{\partial \phi_i}{\partial t} = \frac{\partial}{\partial x}\left[\sum_j^{p,n}\left(D_{ij}\frac{\partial \phi_j}{\partial x} - B_{ij}\frac{\partial^3 \phi_j}{\partial x^3}\right)\right] \quad (10)$$

where

$$D_{pp} = D_0\left[\frac{1-\phi_p}{N} + \phi_p - \phi_n\phi_p\chi_{pn}\right] \quad (11a)$$
$$D_{pn} = D_0\left[\phi_p(1-\phi_p)\chi_{pn}\right] \quad (11b)$$
$$D_{np} = D_0\left[\phi_n(1-\phi_n)\chi_{pn}\right] \quad (11c)$$
$$D_{nn} = D_0\left[1-\phi_n\phi_p\chi_{pn}\right] \quad (11d)$$

are the components of the Fickian diffusion matrix,

$$B_{pp} = D_0\kappa\left[\phi_p(1-\phi_p)\right] \quad (12a)$$
$$B_{pn} = -D_0\kappa\left[\phi_p\phi_n\right] \quad (12b)$$
$$B_{np} = -D_0\kappa\left[\phi_p\phi_n\right] \quad (12c)$$
$$B_{nn} = D_0\kappa\left[\phi_n(1-\phi_n)\right] \quad (12d)$$

are the components of the gradient coefficient matrix and $D_0 = k_BT/\zeta_0$ is the monomer diffusion coefficient.

The thin-film geometry is formally described by initial and boundary conditions that supplement Equations 10–12. We take the initial condition for each species to be a scaled step-function,

$$\phi_i(x, t=0) = (\phi_i^{\mathrm{b}} - \phi_i^{\mathrm{f}})\theta(x) + \phi_i^{\mathrm{f}} \quad (13)$$

where $\theta(x)$ is the step function, ϕ_i^{b} are the initial volume fractions in the bath and ϕ_i^{f} are the initial volume fractions in the thin film. Due to the fourth-order gradient, the semi-infinite geometry includes two boundary conditions at a (substrate) wall at $x = -l_{\mathrm{f}}$ and two at $x \to \infty$. At the wall, we have a mass-conserving, no-flux condition

$$\sum_j M_{ij}\left.\frac{d\mu_j}{dx}\right|_{x=-l_{\mathrm{f}}} = 0 \quad (14)$$

and a condition imposing thermodynamic equilibrium at the surface

$$\left.\frac{df_w}{d\phi_i} + \kappa\frac{d\phi_i}{dx}\right|_{x=-l_{\mathrm{f}}} = 0. \quad (15)$$

In the latter boundary condition, f_w is the surface free energy density[20,21] given by

$$f_w = \chi_{wp}\phi_p(x=-l_{\mathrm{f}}) + \chi_{wn}\phi_n(x=-l_{\mathrm{f}}) \quad (16)$$

where χ_{wp} and χ_{wn} are effective wall-polymer and wall-nonsolvent interactions, which are assumed zero unless otherwise noted. Using this form for f_w, the second boundary condition becomes a prescription of the local contact angle

$$\left.\frac{d\phi_i}{dx}\right|_{x=-l_{\mathrm{f}}} = -\frac{\chi_{wi}}{\kappa}. \quad (17)$$

The conditions at infinity are given by

$$\lim_{x\to\infty}\phi_i = \phi_i^{\mathrm{b}} \quad (18)$$
$$\lim_{x\to\infty}\frac{d\phi_i}{dx} = 0. \quad (19)$$

The Dilute Limit

In the case that both the bath and the film are mostly solvent ($\phi_p^b \ll 1$, $\phi_n^b \ll 1$ and $\phi_p^f \ll 1$, $\phi_n^f \ll 1$), transport occurs far away from the binodal, and no phase separation dynamics are relevant. Eq. 10 then reduces to a set of uncoupled, constant-coefficient diffusion equations,

$$\frac{\partial \phi_i}{\partial t} = D_i\frac{\partial^2 \phi_i}{\partial x^2} \quad (20)$$

with the initial condition in Eq. 13 and the simplified boundary conditions

$$\left.\frac{d\phi_i}{dx}\right|_{x=-l_\mathrm{f}} = 0 \tag{21}$$

$$\lim_{x\to\infty} \phi_i = 0 \tag{22}$$

where $D_p = \frac{k_B T}{\zeta_0 N}$ and $D_n = \frac{k_B T}{\zeta_0} = D_0$. Note that this limit is singular, with the fourth order derivative and additional boundary terms disappearing.

Eq. 20 readily yields an analytical solution,

$$\frac{\phi_i(x,t) - \phi_i^\mathrm{b}}{\phi_i^\mathrm{f} - \phi_i^\mathrm{b}} = \frac{1}{2}\left[\mathrm{erf}\left(\frac{x+2l_\mathrm{f}}{2\sqrt{D_i t}}\right) - \mathrm{erf}\left(\frac{x}{2\sqrt{D_i t}}\right)\right]. \tag{23}$$

It is convenient to introduce a dimensionless variable $\xi_i \equiv x/(\sqrt{2D_i t})$ into Eq. 23, giving

$$\frac{\phi_i(x,t) - \phi_i^\mathrm{b}}{\phi_i^\mathrm{f} - \phi_i^\mathrm{b}} = \frac{1}{2}\left[\mathrm{erf}\left(\frac{\xi_i}{\sqrt{2}} + \frac{l_\mathrm{f}}{\sqrt{D_i t}}\right) - \mathrm{erf}\left(\frac{\xi_i}{\sqrt{2}}\right)\right]. \tag{24}$$

When the film is thicker than the diffusion length ($l_\mathrm{f} \gg \sqrt{D_i t}$) or the time is shorter than the diffusion time ($t \ll l_\mathrm{f}^2/D_i$) the argument of the first error function on the right-hand side of Eq. 24 approaches infinity, giving the infinite domain solution,

$$\lim_{tD_i/l_\mathrm{f}^2\to 0} \frac{\phi_i(x,t) - \phi_i^\mathrm{b}}{\phi_i^\mathrm{f} - \phi_i^\mathrm{b}} = \frac{1}{2}\left[1 - \mathrm{erf}\left(\frac{\xi_i}{\sqrt{2}}\right)\right]. \tag{25}$$

There are two important physical consequences in this limit. First, the film thickness drops out of the equation entirely, and transport is completely independent of it. Second, distance and time collapse with the similarity variable $\xi \sim x/\sqrt{t}$ and when scaled properly, the solution is stationary in a self-similar shape. At long times, neither of these properties are guaranteed. The film thickness becomes an important length scale and the concentration profile is no longer self-similar.

Asymptotic analysis

Non-dimensionalizing Eq. 10 permits an asymptotic analysis that provides some important insights. Choosing the length scale l_f and timescale l_f^2/D_0 gives,

$$\frac{\partial \phi_i}{\partial \tilde{t}} = \frac{\partial}{\partial \tilde{x}}\left[\sum_j^{p,n}\left(\tilde{D}_{ij}\frac{\partial \phi_j}{\partial \tilde{x}} - \epsilon^2 \tilde{B}_{ij}\frac{\partial^3 \phi_j}{\partial \tilde{x}^3}\right)\right] \tag{26}$$

where $\tilde{x} = x/l_\mathrm{f}$, $\tilde{t} = D_0 t/l_\mathrm{f}^2$, $\tilde{D}_{ij} = D_{ij}/D_0$, $\tilde{B}_{ij} = B_{ij}/(D_0\kappa)$ and $\epsilon = \sqrt{\kappa}/l_\mathrm{f}$. The dimensionless quantity ϵ is very small since κ is a mesoscale parameter and l_f is a macroscopic parameter.

To our knowledge an asymptotic analysis of the multi-component model Eq. 26 has not been presented in the literature to date. Due to its difficulty, a comprehensive analysis of this singular, multi-scale, multi-region matched asymptotics problem is beyond the scope of the present paper. However, a classic paper by Pego[22] presents results for the binary Cahn-Hilliard model,

$$\frac{\partial \phi}{\partial t} = \nabla^2\left[f_0'(\phi) - \epsilon^2\nabla^2\phi\right] \tag{27}$$

in an unbounded domain where $f_0'(\phi)$ is an unspecified homogeneous free energy. Despite the difference in the number of components and boundary conditions, we expect many qualitative results to be the same between the two models. As such, we describe Pego's relevant findings in light of our model.

Pego assumes initial conditions that lead to phase-separation (but are not necessarily at equilibrium) and subsequently divides his analysis into an inner region that encompasses the interface and two outer regions that correspond to our film and bath (cf. Figure 2). He identifies four relevant time scales, and we will briefly discuss the behavior in the inner and outer regions at each scale.

The smallest time scale is $\tilde{t} \sim \epsilon^2$, which corresponds to $t \sim \kappa/D_0$ in dimensional units in our model. At this scale, the leading order outer regions (i.e. bath and film) remain unchanged from their initial values, while the inner region (the interface) undergoes rapid equi-

libration. The equilibrium values reached at the interface ($\phi_i^{eq,+}$ and $\phi_i^{eq,-}$) are due to the local initial condition and are not in general equal to the concentrations in the outer regions (ϕ_i^{f} and ϕ_i^{b}).

Subsequently, boundary layers form between the equilibrated interface and the outer regions to "match" the inner and outer solutions. The evolution of the boundary layers occurs on time scales between $\epsilon^2 \ll \tilde{t} \ll 1$ which corresponds to $\kappa/D_0 \ll t \ll l_{\mathrm{f}}^2/D_0$ in dimensional units. As expected the size of the boundary layers are proportional to $t^{1/2}$ and the solution for the outer region is described by a similarity solution that collapses with a single variable $\tilde{x}/(2\tilde{t})^{1/2}$. Note the qualitative similarities between Pego's analysis at this scale and the full solution for the dilute regime described above. Both include similarity variables, but the matched asymptotic scheme accounts for a phase separated interface whereas the solution in the dilute regime is complicated by a finite film thickness and two time scales coming from the differing diffusivities of polymer and nonsolvent.

At the time scale $\tilde{t} \sim 1$ or $t \sim l_{\mathrm{f}}^2/D_0$ in dimensional units, diffusive exchange happens across the interface, and the film shrinks or swells. Here, the leading order terms in the phase field model are equivalent to a classic Stefan problem,[22,23] where the inner solution is in local equilibrium and the boundary layers in the outer solution are large compared to l_{f}. In the classic formulation of the Stefan problem, sustained diffusive exchange is driven by boundary conditions, but in our case the semi-infinite nonsolvent bath serves the same purpose. Finally, at this time scale Pego predicts an interface velocity that is proportional to the difference in the chemical potential gradient across the interface (i.e. the mass flux), and ultimately approaches zero when $\tilde{t} \gg 1$.

The fourth and largest time scale in the asymptotic expansion is $\tilde{t} \sim 1/\epsilon$ or $t \sim l_{\mathrm{f}}^3/(D_0\kappa^{1/2})$ in dimensional units. At this scale both the inner and outer solutions are in quasi-equilibrium, and the interface moves due to chemical potential gradients arising from interface curvature. This phenomena is perhaps most familiar in the Ostwald ripening/coarsening process that occurs in mixtures of immiscible liquids. We expect that this final time scale will be of lesser import at the bath/film interface than the previous three. However, Ostwald ripening can certainly occur inside precipitating films following phase separation.

Surface-directed spinodal decomposition

Finally, we briefly highlight the theory of surface-directed spinodal decomposition and its application to the current system. In the bulk, spinodal decomposition driven by a temperature quench proceeds isotropically, and a linear stability analysis may be used to obtain the fastest growing domain size immediately following phase separation.[15] However, when symmetry is broken by a surface, spinodal decomposition is no longer isotropic and proceeds via a wave traveling from the interface into the bulk of the film.[12,24] Ball and Essery showed that this traveling spinodal wave occurs when either (i) the bulk temperature is *below* the spinodal temperature T_s and there is a surface energy, or (ii) the bulk temperature is *above* the spinodal temperature T_s and the surface temperature is suddenly dropped below T_s.[12]

Examining the perturbations about a homogeneous state in a semi-infinite domain, Ball and Essery[12] derived an expression for a traveling wave solution of a binary Cahn-Hilliard fluid quenched at the surface into the spinodal region. However, as was the case with the asymptotic analysis by Pego in the previous section, we are not aware of parallel calculations for a ternary Flory-Huggins phase-field model, i.e. Eq. 10 with appropriate initial and boundary conditions. Nevertheless, while some quantitative details may differ, we expect that a traveling wave solution in the Flory-Huggins model will be qualitatively identical to that of the Cahn-Hilliard model. More quantitative details related to surface-directed spinodal decomposition can be found in the Supplemental Information.

Results and Discussion

Pego's asymptotic analysis and the dilute solution theory outlined above suggest an important division at the timescale $\tau = l_f^2/D_0$, the characteristic time it takes the non-solvent to diffuse to the bottom of the film. Theory suggests that at times much less than τ, the behavior at or near the interface dominates, and since these are largely determined by the initial conditions, the film thickness is inconsequential. By contrast, at times much larger than τ, solvent/nonsolvent exchange drives a change in the film concentration, with the film thickness playing an important role.

To test this hypothesis, we performed a series of one-dimensional simulations where we varied the film thickness (l_f = 51.2, 102.4, 204.8 in units of the polymer end-to-end distance, R_0) and degree of polymerization (N_p = 10, 20, 50) and examined the non-solvent concentration at the bottom of the film (i.e. the wall). All simulations were performed in 1D with Flory-Huggins parameters given by: χ = 1.213, κ = 3.369 (for N_p = 10), χ = 1.048, κ = 2 (for N_p = 20), and χ = 0.9120, κ = 12.67 (for N_p = 50). The initial bath concentration is essentially pure nonsolvent: $\phi_p^b = 0.01$, $\phi_n^b = 0.98$ (where a finite solvent and polymer concentration are required for numerical stability), and the initial film concentration was chosen far enough away from the phase envelope that the film does not immediately precipitate: $\phi_p^f = 0.204$, $\phi_n^f = 0.301$.

The results of these simulations presented in Figure 3(a), show that the nonsolvent concentration at the wall remains unchanged for some delay period and then begins to increase monotonically. Figure 3(b) shows the same data rescaled by the diffusion time. In the latter, all of the data collapse to a single curve, illustrating that the diffusion time is indeed the timescale governing the transition thereby confirming the qualitative results of the dilute solution theory.

Having confirmed that the transport behavior differs based on the timescale τ, we break our remaining analysis into two parts. In the section that immediately follows, we examine early-time behavior ($t \ll \tau$), specifically focusing on films that precipitate on this timescale. Subsequently, we turn our attention to late-time behavior ($t \gg \tau$) and the characteristics of mass-transport driven phase separation in that regime.

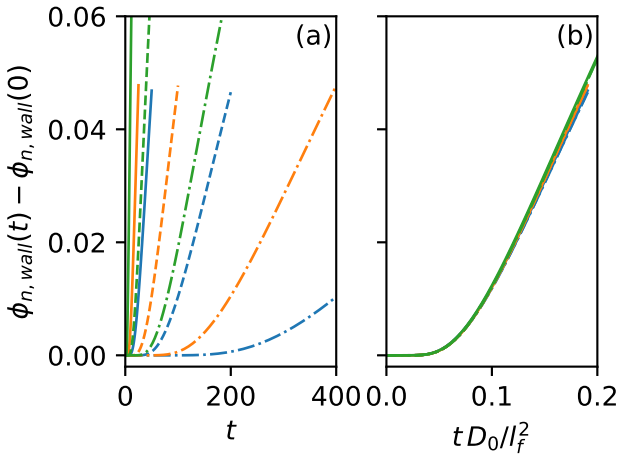

Figure 3: Nonsolvent concentration at the wall versus time for three different values of the film thickness: l_f = 51.2 (solid), 102.4 (dashed), 204.8 (dot-dashed) and three different degrees of polymerization: N_p = 10 (blue), 20 (orange), 50 (green). (a) Concentration versus raw simulation time-units (the Rouse time of the polymer).[15] (b) Concentration versus time scaled by the diffusion time, τ.

Early-Time Regime

A key theoretical prediction in the early-time regime is an insensitivity of the mass-transport behavior to the film thickness. In fact, Pego predicts that the concentration profile in this time regime, $\kappa/D_0 \ll t \ll l_f^2/D_0$, will be self-similar.

We verify that the concentration profiles in our simulations are indeed self-similar at early times in Figure 4. As discussed previously, we perform a series of one-dimensional simulations where we vary the film thickness, but in this case we examine the entire volume fraction profile at early times before the nonsolvent boundary layer can reach the bottom of the film. In Figure 4 we show results for three simulations where N_p = 20, κ = 2, χ_{pn} = 1.048, $\phi_p^f = 0.301$, $\phi_n^f = 0.01$, $\phi_p^b = 0.01$, $\phi_n^b = 0.98$

and $l_f = 51.2$, 102.4, and 204.8 at $t = 2.5$, 10, and 40 respectively. Panel (a) shows the unscaled data, zoomed in near the interface, and panel (b) shows the same data that now collapses when rescaled by the similarity variable $\xi = \xi_0 = x/\sqrt{2D_0 t}$.

Figure 4(c) shows the same three profiles as panels (a) and (b) plotted in composition space alongside the ternary phase diagram. Such a plot has historically been called a "composition path",[5,6] and as is evident in the figure, this path is insensitive to the film thickness at early times.[1] Additionally, the composition path is stationary in time for $t \ll l_f^2/D_0$, i.e. as long as the nonsolvent boundary layer has not yet reached the bottom of the film.

The properties of thickness independence and stationarity narrow the range of possible behaviors of early-time composition paths, but they remain very sensitive to the initial film concentration. To examine this behavior, we performed one-dimensional simulations while varying the initial film concentration and holding the bath concentration constant at nearly pure nonsolvent ($\phi_p^b = 0.01$, $\phi_n^b = 0.98$). All of the relevant 1D simulations for this study were performed with $N_p = 20$, $\kappa = 2$ and $\chi_{pn} = 1.048$.

We observe three regimes of behavior depending on the location of the initial film concentration in composition space. Figure 5(a) shows a representative simulation in each of the regimes and Fig. 5(b) categorizes the behavior of a sweep of initial film compositions in composition space alongside the ternary phase diagram. In regime I the composition path does not cross into the two phase region, so no phase separation occurs and the interface remains diffuse. In regime II the composition path crosses into the two phase region, resulting in a phase separation into two domains, a polymer-rich film and polymer-lean bath, with boundary layers at the

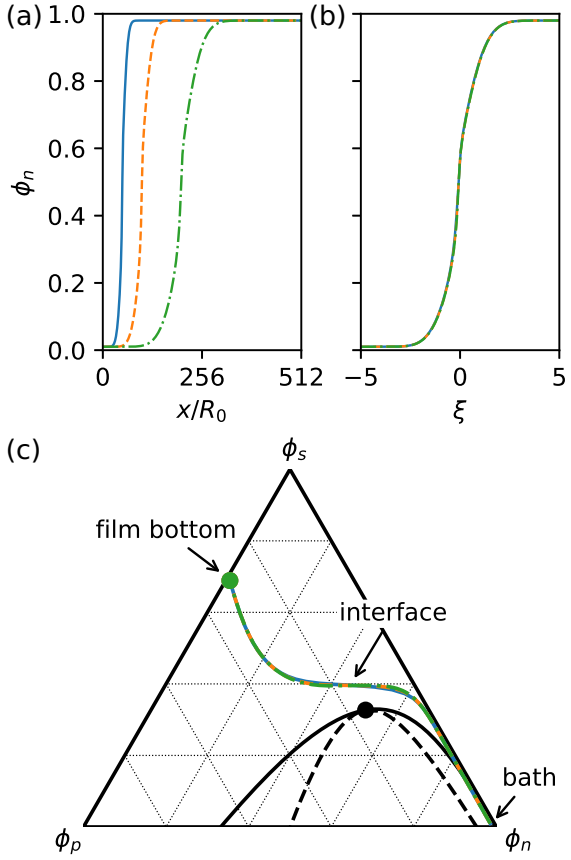

Figure 4: Early-time nonsolvent concentration for a 1D simulation with different film thicknesses as a function of (a) space, (b) similarity variable and (c) composition. Both the similarity variable and composition-space plot collapse the data.

edge of each interface. Regimes I and II are not very interesting at early times, however, as we discuss in the next section, they can both lead to a delayed precipitation at later times.

By contrast, regime III is a more interesting example of non-equilibrium phase behavior; films prepared with initial conditions in this regime are stable when isolated at equilibrium, but are unstable immediately following contact with the nonsolvent bath. Here, the composition path plunges directly into the spinodal, the phase separation kinetics break stationarity and waves of spinodal decomposition propagate into the film as time progresses. In fact, regime III appears to be the mass-transfer analogue of classic temperature-driven surface-directed spinodal decomposition.[12]

It is insightful to compare the results of our

[1] Originally, the term "composition" path referred only to the early-time composition, where, because of similarity, one could interpret the curve as simultaneously representing both spatial and temporal film compositions. However, the term has been used much more broadly as simply the volume fraction profile plotted in composition space with real space being implicit. We use the term in this latter sense.

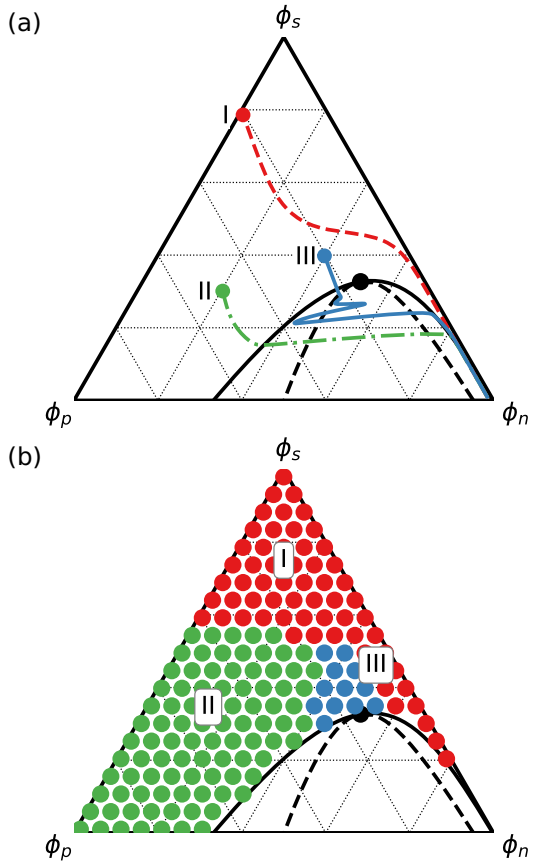

Figure 5: (a) Representative composition paths of three different regimes of behavior plotted in composition space alongside the phase diagram. Regime I (red dashed line) shows no phase separation between bath and film, Regime II (green dot-dashed line) shows a sharp interface between the bath and film and Regime III (blue solid line) shows an immediate spinodal decomposition of the film. (b) Phase plot of initial film concentrations which give rise to each regime: I (red), II (green), III (blue).

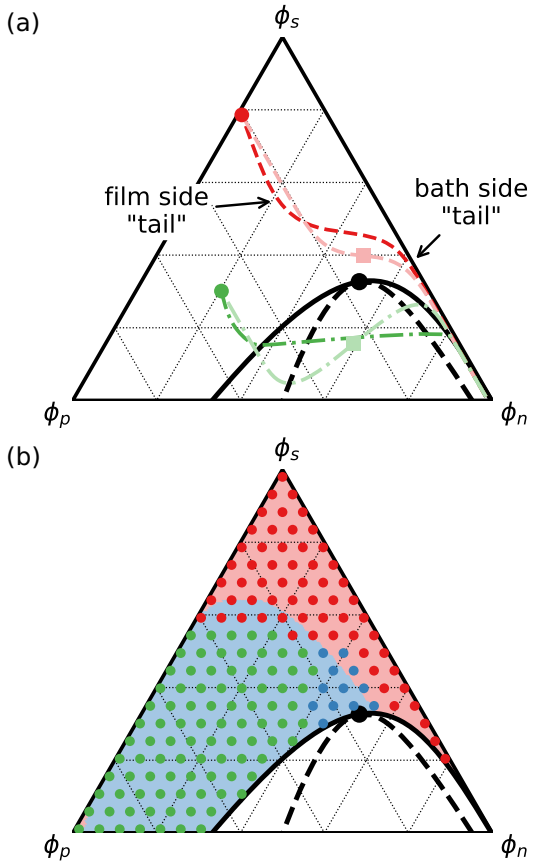

Figure 6: (a) Comparison between composition paths from simulation (regime I: dark red dashed line, regime II: dark green dot-dashed line) and from dilute solution theory (regime I: light red dashed line, regime II: light green dot-dashed line). (b) Comparison between regimes I (red circles, no phase separation), II (green circles, phase separation) and III (blue circles, surface-directed spinodal decomposition) determined from simulation data and the location of the midpoint of the interface of the initial condition. Initial compositions where the midpoint of the interface falls within the spinodal are shaded blue and those that fall outside the spinodal are shaded red.

1D simulations with some of the theoretical predictions outlined above. Figure 6(a) compares the composition paths from our 1D simulations for regimes I and II with the "dilute-limit" prediction. As one might expect, the dilute-limit theory does poorly for regime II where phase separation occurs and fails completely for regime III. However, even regime I with a relatively dilute initial polymer concentration in the film is not well described by the theory.

Repeated tests with equations of the form of Eq. 25 show that the length of the "tails" of the composition path are determined by the relative diffusivity of the polymer and nonsolvent. A relatively slow polymer diffusion coefficient gives longer tails parallel to the polymer composition line, whereas equal diffusion coefficients gives a straight-line composition path between the film and bath with no tails. Additional testing reveals that the location of midpoint of the composition path, i.e. the red and green square in Figure 6(a), is fixed regardless of the

diffusivity. From these tests we conclude that a concentration-dependent diffusivity is critical to predicting the early-time composition path regardless of whether or not the film phase separates initially.

It would also be desirable to have an easy way to predict the regime of behavior from the initial condition without having to run a full simulation. Based on Pego's analysis, we expect that the early-time phase separation behavior will be determined by the local initial concentration near the interface. Accordingly, we hypothesize that if the midpoint of the interface of the initial condition, i.e. the average of the initial bath and film concentrations, is within the spinodal, we will observe phase separation. Recall that we have neglected thermal fluctuations in our model, so an interface inside the binodal but outside the spinodal would not be able to cross the nucleation barrier to show a phase separation.

Figure 6(b) compares this simple prediction with the full simulation results. As in Figure 5(b), the initial conditions which give rise to the three different regimes are marked by different colored points and the prediction is marked by background shading. The interface-midpoint prediction is centered in roughly the right place in composition space, but does not accurately predict the curvature of the border between the two regions. However, considering the crudeness of the prediction, the correspondence with the full calculation is surprisingly close.

Unfortunately, we do not have a simple metric for distinguishing between regimes II and III. The upper left tail of the composition path represents the concentration on the film side of the interface, and repeated observations of simulation data suggests that one observes regime III when this tail crosses into the spinodal region. By contrast, one observes regime II when a different part of the composition path enters the spinodal. Because polymer diffusion is slow, and the composition path is nearly parallel to lines of constant polymer composition, regime III tends to occur to initial conditions that are located north-northwest of the spinodal and regime II typically appears due west. Regrettably, these insights are qualitative and difficult to use to make a simple quantitative prediction.

One can gain additional insight into the kinetic regimes by examining the effects of model parameters, which is explored in detail in the Supplemental Information. Figure S2 categorizes the kinetic regimes of several different data sets by their initial condition by systematically varying N_p, χ_{pn} and χ_{ns}. Upon varying these parameters, we find results consistent with our qualitative interpretations discussed above. Specifically, the data support our conclusions that the initial local concentration of the interface is primarily responsible for distinguishing regime I from regime II and that the entrance of the film-side "tail" of the composition path into the spinodal is responsible for a film that undergoes spinodal decomposition.

Finally, we are able to perform 2D and 3D simulations to examine the microstructure and hydrodynamics of regime III. We recently reported unique hydrodynamic behavior of regime III in another publication, including an examination of the possibility that a Marangoni instability that could be responsible for macrovoid formation.[25] Here, we focus on the microstructural evolution absent hydrodynamics.

Figure 7 shows results from 2D and 3D simulations, with exactly the same parameters and initial conditions as the 1D simulations shown in Figure 5. As is the case in 1D simulations, the phase separation starts at the top of the film and proceeds as a travelling wave into the bulk. Initial conditions with a larger solvent concentration result in a shallower quench with larger domain sizes and broader interfaces, whereas quenches nearer the spinodal line are deeper with smaller domain sizes and sharper interfaces.

The characteristics of the morphology that develops depends on the polymer concentration of the film, following a qualitatively similar pattern to isotropic spinodal decomposition. At high polymer concentration, we observe nonsolvent-rich droplets in a polymer matrix, and at low polymer concentration we observe the inverse morphology: polymer-rich

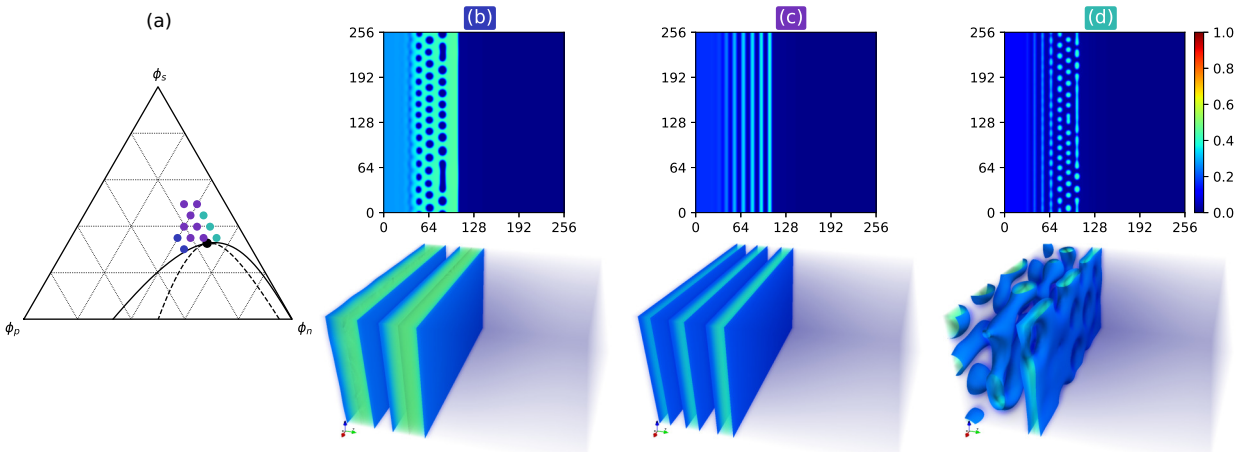

Figure 7: (a) The part of the composition space exhibiting regime III colored by the observed microstructure in 2D simulations: non-solvent droplets in a polymer matrix (blue), alternating bands of polymer and nonsolvent (purple) and polymer droplets in nonsolvent (blue-green). 2D contour plots ($256R_0 \times 256R_0$) and 3D density plots ($64R_0 \times 64R_0 \times 32R_0$) of the polymer concentration showing microstructure: (b) nonsolvent droplets, (c) alternating bands and (d) polymer droplets. The color bar on the right of (d) indicates polymer concentration and is valid for both 2D and 3D plots.

droplets form in a nonsolvent solution. The center of the region gives alternating bands of polymer and nonsolvent. Because our simulations neglect thermal fluctuations, it is necessary to add random noise to the initial conditions to observe droplets. Subsequently, the exact crossover between different microstructures is sensitive to the strength of the applied noise. Also, note that the morphology is a function of time; immediately following phase separation, coarsening processes cause domain coalescence and growth.

Though the sequence is qualitatively similar, the morphologies in Figure 7 are not identical to isotropic spinodal decomposition. In lieu of random isotropic droplets patterns or a bicontinuous morphology, the travelling spinodal wave gives hexagonally ordered droplets[26] and striped domains. We suspect however, that some or all of this order will disappear for systems with thermal fluctuations. Additionally, diffusion leads to an inhomogeneous concentration at the top of the film, often giving an enhanced polymer concentration at the interface. In many cases, this leads to a thin polymer-rich region at the top of the film, even at low overall polymer concentration. Nevertheless, sometimes this thin domain is transient and breaks up as the phase separation proceeds.

Finally, there are some differences between the 2D and 3D morphologies. In Fig. 7(b) 2D simulations show nonsolvent droplets in a polymer matrix, whereas 3D simulations show thick bands. Based on our experience, we attribute this disparity to either the relatively small size of the 3D simulation box or to a difference in the impact of the initial noise strength on 2D versus 3D simulations. Future work with larger simulation boxes and with models that include thermal fluctuations will therefore be necessary to provide greater insight. Fig. 7(d) also shows a difference in morphology; 2D simulations show polymer droplets, whereas the 3D simulations show connected, elongated polymer domains. Notably, the 3D simulations show a banded structure, but no hexagonal ordering. This difference is clearly a consequence of dimensionality and suggests that we might expect to find isolated polymer droplets at yet lower polymer concentrations. Unfortunately, we did not observe this morphology in our limited set of 3D simulations.

Late-Time Regime

At times $t \gg l_f^2/D_0$ the concentration at the bottom of the film changes, meaning the concentration profiles are no longer self-similar and the composition paths are no longer stationary. A typical case of the time evolution of the composition profile is given in Figure 8. Here, we present long-time simulations with the same thermodynamic and kinetic parameters and initial compositions as the short-time data in Figure 4, i.e. $N_p = 20$, $\chi_{pn} = 1.048$, $\kappa = 2$ with $\phi_p^f = 0.3$, $\phi_n^f = 0.01$, $\phi_p^b = 0.01$ and $\phi_n^b = 0.98$. Figure 8(a) shows the volume fraction of the nonsolvent versus the similarity variable at four different time-points, and Figure 8(b) show the same data plotted in composition space alongside the ternary phase diagram.

The data in Figure 8 shows an invariance to the film thickness that is worth noting. Simulations for both $l_f = 102.4$ and $l_f = 51.2$ show equivalent behavior in both real and composition space when the time is chosen such that $t_1/t_2 = (l_{f,1}/l_{f,2})^2$. This invariance and choice of t can be understood by recalling Eq. 24, a result of our dilute solution theory. In the theory, late-time diffusion is governed by two variables, either the dimensional quantities x and t or the dimensionless groups, ξ and tD_0/l_f^2. This result is especially useful, because in many cases it removes film thickness as an independent variable that needs to be accounted for in the simulations. Notably, when other kinetic processes such as spinodal decomposition are present, additional time scales may be relevant and the dimensional analysis discussed above is incomplete. However, we show in Figure S3 in the Supplemental Information, that this is a minor issue and that the nonsolvent/solvent transport remains largely the same, independent of whether or not spinodal decomposition takes place.

We observe several stages of behavior in the concentration profiles in Figure 8. Stage (i) is the early-time profile discussed above (c.f. Figure 4). These initial conditions provide an example of the previously discussed early-time regime I, where no immediate phase separation occurs. Stage (ii) occurs when a portion of

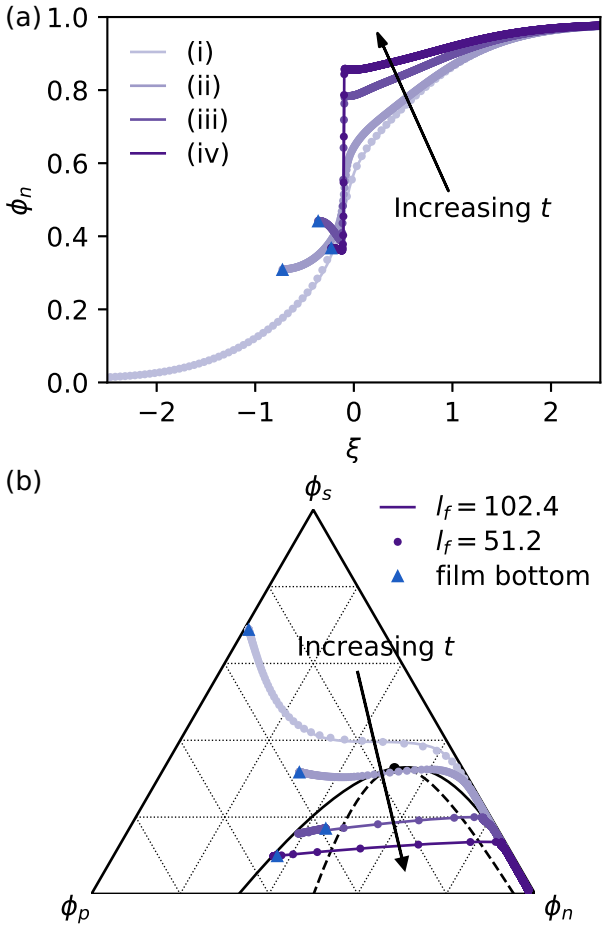

Figure 8: (a) Real-space and (b) composition-space volume fraction profiles of long-time, 1D simulations of solvent-nonsolvent exchange. The solid curves show a film thickess of $l_f = 102.4$ at time points (i) 10, (ii) 500, (iii) 2×10^3, and (iv) 5×10^3 (in units of the Rouse time). The closed circles show a film thickness of $l_f = 51.2$ at time points (i) 2.5, (ii) 125, (iii) 500, and (iv) 1.25×10^3.

the concentration profile crosses the plait point into the two-phase region. This transition point marks the beginning of phase separation, and a true interface develops between the bath and the film where the interface composition is determined by a local equilibrium.

Stage (iii) is characterized by mature phase separation between the bath and film and an inhomogeneous concentration profile in the polymer film. As solvent-nonsolvent exchange proceeds, the concentration of the interface follows the binodal curve, deepening the quench. As seen by the marker denoting the bottom of the

film, the composition of the rest of the film trails the composition of the interface, giving an enhanced polymer concentration and depleted non-solvent concentration at the interface relative to the bulk of the film. Eventually, in stage (iv) the time scales are large enough for diffusion to create a nearly homogeneous film whose concentration is again determined by a local equilibrium condition.

To get a sense of the time scales, notice the logarithmic spacing between the time points of the various stages. Phase separation occurs relatively quickly following the early-time regime, but diffusion across a stable interface appears to take place over an order of magnitude larger time scale. Similarly, it takes another order of magnitude for the film to become homogeneous. Accordingly, we expect that solvent-nonsolvent exchange will eventually terminate as the system equilibrates, but it would take a remarkably long simulation to observe.

As is the case with the early-time results, the system dynamics at later times depend strongly on the location of the initial condition in composition space. Previously, we observed three different regimes of qualitative behavior: (I) no phase separation, (II) simple phase separation characterized by a single interface between the bath and film and (III) spinodal decomposition of the film. Now we observe these same three regimes again, but transitions can occur between the early-time regime and the late-time regime as solvent/nonsolvent exchange progresses.

Figure 9 shows results for a series of long-time, 1D simulations with $N_p = 20$, $\chi_{pn} = 1.048$ and $\kappa = 2$. Markers are placed at each initial film composition where a simulation was run, and as before, the color of the marker indicates qualitative behavior at late times. Red markers denote initial compositions which result in regime I behavior (no phase separation), green markers denote regime II (simple phase separation) and blue markers denote regime III (spinodal decomposition). Additionally, as demonstrated in Figure 8, solvent/nonsolvent exchange can result in a composition path that transitions from one regime at early times to another at late times. Figure 9 characterizes

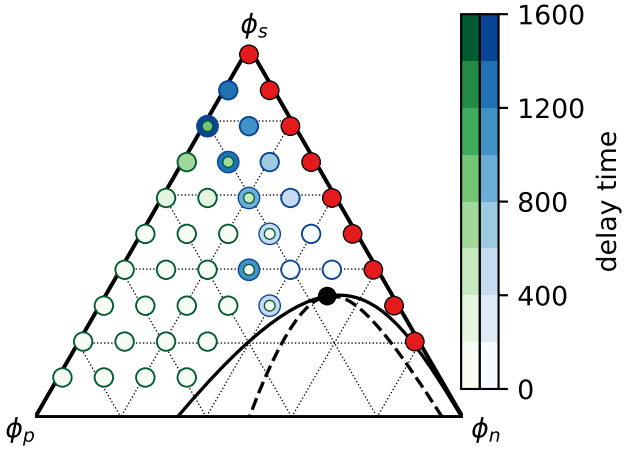

Figure 9: Characterization of the late-time phase separation behavior according to the initial film composition. Red circles indicate no phase separation (regime I). Green circles indicate simple phase separation (regime II), where the shade of green denotes the delay time before the onset of phase separation. Blue circles indicate spinodal decomposition (regime III), where the shade of blue denotes the delay time. As indicated, some film compositions in the middle of the phase diagram transition between regimes II and III.

these transitions with a delay time, i.e. the simulation time that passes before a regime is observed. The delay time is shown in the figure via shading, with darker colors indicating a longer delay.

The kinetic behavior summarized in Figure 9 is relatively complex, and we find seven qualitatively different scenarios that a composition path can take.

1. *Early-time regime I to late-time regime I.* This scenario occurs for all of the red circles on the far right-hand side of the phase diagram. Here, the polymer concentration is too low for any phase separation to occur, even at long times.

2. *Early-time regime II to late-time regime II.* This scenario occurs for all of the white circles outlined in green (i.e. zero delay time) on the lower left-hand side of the phase diagram. This is the opposite case of scenario 1; the polymer is so concen-

trated that spinodal decomposition of the film is impossible.

3. *Early-time regime III.* This scenario occurs for the white circles outline in blue (i.e. zero delay time) near the critical point that undergo immediate spinodal decomposition.

4. *Early-time regime I to late-time regime II.* This scenario occurs for the green circles with a finite delay time. Here the polymer concentration is just low enough that solvent/nonsolvent exchange can drive a film that is not initially phase separated to form a sharp interface with the bath, but the polymer concentration is too large for the film to enter the spinodal.

5. *Early-time regime I to late-time regime III.* This scenario occurs for the blue circles with a finite delay time. Solvent/nonsolvent exchange drives these composition paths directly into the spinodal after a delay time that increases as the solvent concentration increases at constant polymer concentration.

6. *Early-time regime II to late-time regime III.* This scenario occurs for the small white circles outlined in green with no delay time surrounded by larger, darker blue circles with a finite delay time. These initial film compositions are close enough to the spinodal that solvent/nonsolvent exchange can drive the film into the spinodal region. However, a modest increase of the solvent concentration at constant polymer composition results in scenarios 2 and 3.

7. *Early-time regime I to late-time regime II to late-time regime III.* This is the most complicated scenario, and occurs for the small green circles with a finite delay time surrounded by larger, darker blue circles. Here the composition path progresses through all three regimes, with no early-time phase separation, but undergoing both a simple phase separation at the interface and later a delayed spinodal decomposition as time progresses. Again, note that the delay time increases as the solvent concentration increases at fixed polymer concentration.

It is clear from Figure 9 that the initial polymer concentration is remarkably predictive of the qualitative dynamics of the mass transfer driven phase separation at late times. We desire to understand why this is so, and if possible, we would also like heuristics about what distinguishes the different late-time kinetic regimes on the phase diagram. We again turn to the dilute-limit, simple diffusion model outlined in the theory section above. By setting $x = -l_{\mathrm{f}}$, the location of the wall, in the long-time solution in Eq. 24, we obtain a prediction for the concentration at the wall as a function of time

$$\phi_i^{\mathrm{wall}}(t) = \phi_i^{\mathrm{b}} + (\phi_i^{\mathrm{f}} - \phi_i^{\mathrm{b}}) \operatorname{erf}\left(\frac{l_{\mathrm{f}}}{2\sqrt{D_i t}}\right). \quad (28)$$

Figure 10(a) shows the results of this prediction for an initial film concentration of $\phi_p^{\mathrm{f}} = 0.3$, $\phi_n^{\mathrm{f}} = 0.01$ with $N_p = 20$, $\chi_{pn} = 1.048$ and $\kappa = 2$ (an example of scenario 4) alongside the results of $\phi_i^{\mathrm{wall}}(t)$ directly from a 1D simulation. The dilute solution model shows diffusion into the spinodal via a path that is very nearly parallel to a line of constant polymer concentration, which is a consequence of the relatively slow polymer diffusivity. By contrast, the simulation data shows a gradual *increase* in the polymer concentration at the bottom of the film as solvent/nonsolvent exchange proceeds, followed by a sudden increase in polymer concentration as it approaches the binodal. We hypothesize that the gradual increase is due to film shrinkage as excess solvent leaves the film, and the sudden increase is driven by a phase separation at the interface. We conclude therefore that our simple model can only reproduce phenomena due to the relative diffusivity (as expected), but cannot account for either a changing film thickness, nor the phase separation behavior.

Despite these differences, it is still insightful to compare a prediction of the location of the late-time regimes from the simple dilute-solution model with those from the full model. Accordingly, Figure 10(b) compares a predic-

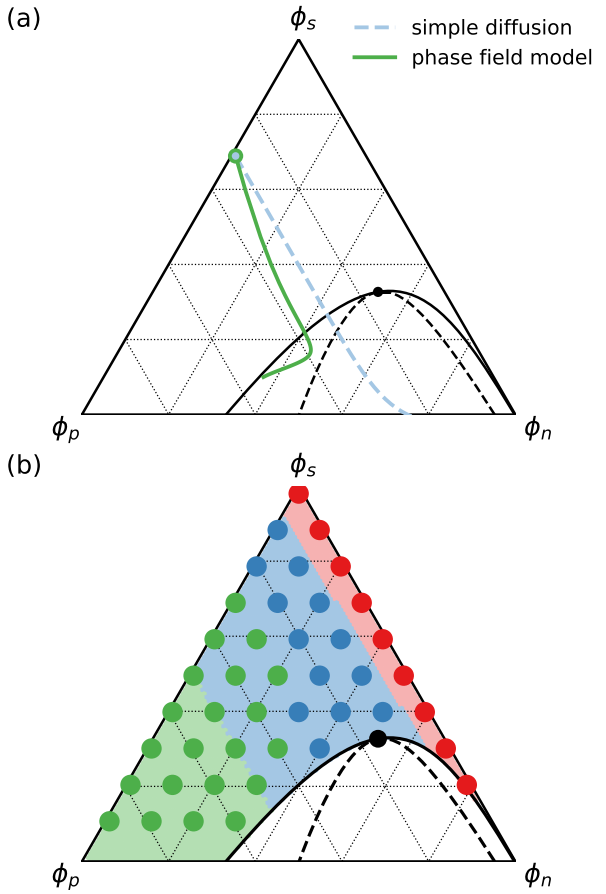

Figure 10: (a) Concentration of the bottom of the polymer film as obtained by Eq. 28 (dashed blue line) and by a 1D simulation of the phase field model (green solid line). Note that this plot shows the wall concentration as a function of time, and does not show a "composition path." (b) Diagram of the infinite delay-time regime (I: red, II: green, III: blue) predicted by Eq. 28 (background shading) and by 1D simulation (dots).

tion of the infinite delay-time regimes from Eq. 28 to the infinite delay-time regimes obtained from simulations of the full 1D model. These predictions were made based on the wall concentration trajectory obtained from Eq. 28. Trajectories that fall to the right of the spinodal envelope do not phase separate and give regime I. Those that fall to the left have an interface that will cross the spinodal, giving regime II, and those that enter the spinodal obviously give regime III. For instance, the simple diffusion trajectory shown in Figure 10(a) is an example of regime III since the concentration clearly enters the spinodal.

Because polymer diffusion is much slower than solvent diffusion, the dilute-limit model predicts trajectories that are nearly parallel to lines of constant polymer composition, and accordingly, so are the regime predictions. As a consequence, any initial condition with a polymer concentration located between the *binary* polymer/nonsolvent spinodal limits gives regime III. The intuition provided by this naive model is that a ternary solution with such a polymer concentration gives regime III at long times because all of the solvent is eventually replaced by nonsolvent.

The simulation data do not agree with this prediction quantitatively, but the differences are instructive. The boundary between regimes I and III is in good agreement with the prediction, indicating that the lower-bound polymer concentration of the binary spinodal is an important threshold. The simulation data also predicts that the boundary between regimes II and III is shifted to the right relative to the prediction from the dilute-solution model. This shift is consistent with the trajectories of the full model in Figure 10(a), where shrinkage and phase separation increase the polymer concentration at the wall, thereby narrowing the window for spinodal decomposition.

Having mentioned it several times, we now turn our attention more fully to the subject of swelling and shrinking of the polymer film. As noted, film swelling and shrinkage plays an important role in determining the concentration of the film as time proceeds, and consequently, has an effect on the microstructure. Furthermore, as the polymer phase solidifies, swelling and shrinking can give rise to mechanical stresses, which have been proposed as a mechanism for the formation of macrovoids in polymer membranes.[27]

Similar to the other kinetic behavior we have observed so far, swelling and shrinking depends on the initial state of the film (in addition to the thermodynamic and kinetic parameters of the system). To examine the impact of the initial conditions, we re-process the raw data used to generate Figure 10 to track the location of the bath/film interface with time. Figure 11(a)

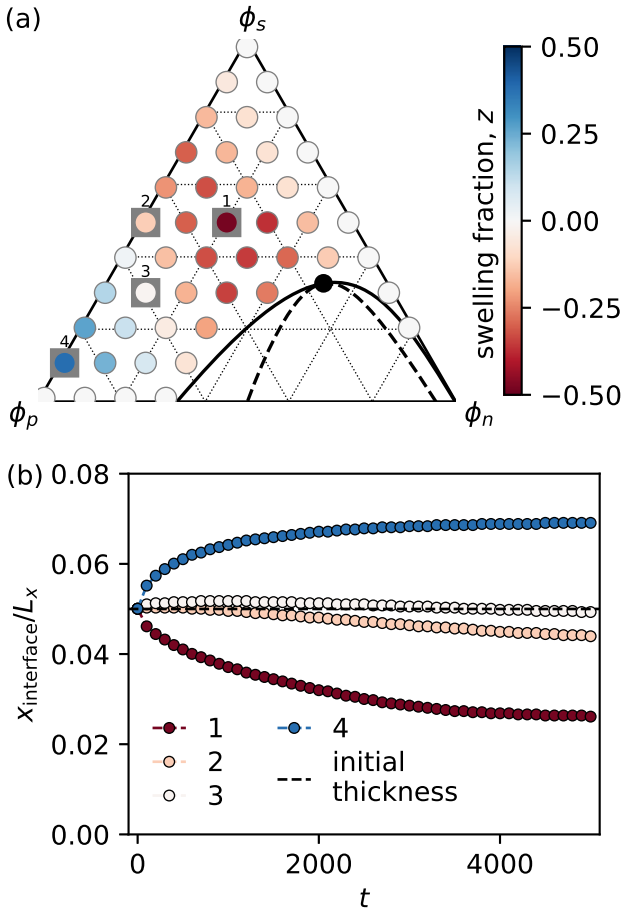

Figure 11: (a) Swelling fraction at $t = 5000$ of a large 1D simulation as a function of the initial film composition, obtained by tracking the interface between the bath and film. (b) Position of the interface versus time for the four specific initial conditions highlighted in panel (a).

shows the swelling fraction,

$$z(t) = \frac{x_{\text{interface}}(t)}{x_{\text{interface}}(0)} \tag{29}$$

at a long time ($t = 5000$ in simulation time) as a function of initial film concentration in composition space alongside the phase diagram. Figure 11(b) shows the time-trajectory of the interface of four of these initial conditions.

At low ϕ_p^{f} (but still above the threshold concentration where the film phase separates), one observes films that shrink, and at high ϕ_p^{f}, the behavior inverts and swelling is observed. Some initial conditions result in substantial swelling and shrinkage. For example, the film prepared in initial condition "1" shrinks nearly 50% of the original film thickness, and the film prepared in initial condition "4" swells by about 50%. Notably, we do not expect experiments to show swelling under the conditions described here, despite the prediction of the model. Instead, we anticipate that despite the driving force to swell, solidification processes (e.g. vitrification) will intervene at large ϕ_p, and the film will arrest.

From the perturbation theory outlined above, we expect film swelling or shrinking to be qualitatively similar to a Stefan problem. Accordingly, we infer that interface motion is the consequence of an imbalance of solvent and nonsolvent flux across the interface, which arises from a contrast between the chemical potential gradients of the two species. Reasoning along these lines, we hypothesize that the observed shrinking at low-to-moderate polymer concentration is due to a difference in miscibility. While the solvent is perfectly miscible in the nonsolvent bath, the nonsolvent is not perfectly miscible in the film because of the presence of the polymer, leading to a relatively smaller driving force (i.e. chemical potential gradient) for the nonsolvent at the interface.

The swelling exhibited at high polymer concentration has a different origin. At large ϕ_p there is very little solvent in the film to begin with, and subsequently very little driving force for solvent to exit into the bath. The swelling observed in this (likely unrealistic) scenario is therefore due to nonsolvent diffusing into the film, driving the concentration towards the binodal line, which is actually at a lower ϕ_p.

From the perturbation theory, we also expect that the interface velocity will be the largest at $t = 0$, and will monotonically approach zero as $t \to \infty$. These features are observed in some trajectories, such as initial conditions 1 and 4 in Figure 11, but not all. For example, initial conditions 2 and 3 in Figure 11(b) are actually non-monotonic, swelling initially before shrinking at long times. We conclude therefore that the analogy to the Stefan problem is only useful as a rough qualitative guide, and the full model must be used to understand the specific shrinking or swelling behavior of an individual

case.

Finally, we examine the microstructure of phase separating films in the late time-regime. Using an expanded set of initial conditions from the 1D simulations in Figure 10, Figure 12(a) gives a ternary diagram with colored dots that mark the qualitatively different microstructures observed in the simulations. Figure 12(b-d) provides representative plots of those microstructures from 2D and 3D simulations.

Figure 12 shows that the microstructure, remarkably, is almost completely dictated by the initial polymer concentration in the film. Figure 12(a) shows three different morphologies for initial conditions inside late-time regime III, with transitions coming along lines nearly parallel to the polymer concentration. Figure 12(b-d) shows that the qualitative features of these morphologies are the same at late times as they are at early times. At low polymer concentration this leads to polymer-rich droplets in nonsolvent crossing over to the inverse morphology of nonsolvent-rich droplets in a polymer matrix at a high concentration. Other morphological features are also similar; a higher initial solvent concentration leads to a more shallow quench (with larger domains and a more diffuse interface), and an inhomogeneous polymer concentration leads to a thin polymer layers at the top of most of the observed morphologies. Additionally, the differences between 2D and 3D simulations are similar to those at early times, with droplet domains becoming elongated and connected in three dimensions.

Thus, despite our lengthy exposition of regimes and kinetic paths, neither the delay time nor the way that the composition path enters the spinodal qualitatively determines the final microstructure. We suspect that this is true only because of the simplicity of our model. Specifically, our diffusive mobility does not arrest at a large polymer concentration, meaning diffusion proceeds normally even if polymer builds up at the interface as may easily happen in regime II. Coarsening also proceeds unhindered by a solidification process, which is also clearly a poor approximation of physical systems.

Concluding Remarks

We have examined the mass-transfer driven process of nonsolvent induced phase separation via a continuum, phase-field model of a ternary polymer solution. It is insightful to put these results into context within the broader experimental and theoretical literature on NIPS. In doing so, we note that our model has not been chosen to quantitatively match any specific polymer/solvent/nonsolvent system. Rather, it represents the simplest possible description of NIPS phenomena, and we seek here to compare to qualitative trends in the literature with the hope of gaining insight into the mechanisms universally shared by all NIPS processes.

In Figure 3, we show that the time it takes the nonsolvent to diffuse the thickness of the polymer film sets a timescale which governs the transition between "early-time" and "late-time" behavior. Additionally, Figures 4 and 8 show that the film thickness can be removed as an independent variable at early times, and can be recast in terms of a similarity variable which is proportional to $t^{1/2}$ at late times.

These results agree with both theoretical and experimental work by McHugh et al.,[6,28–30] who were early pioneers of 1D NIPS mass transfer models (without phase separation kinetics). The dimensional analysis of our simple diffusion model in Eq. 10 is equally applicable to their diffusion-only models.[6] In addition to their early modeling work, McHugh and coworkers used optical techniques to measure the concentration of solvent/nonsolvent in precipitating membranes on both the bath and film side of the interface.[28] On the film side, they observe a diffusive front of nonsolvent moving into the membrane with a velocity that scales like $t^{1/2}$ as predicted.[28,30] This observation of diffusive scaling leads directly to the same invariance of their precipitation experiments to film thickness that we observe in our model. However, in these experiments the same scaling does not apply on the bath side, which leads McHugh et al. to conclude that convection dominates the transport in the bath.[29] We have not tested this hypothesis, but such a calculation could be done in the future using the model and

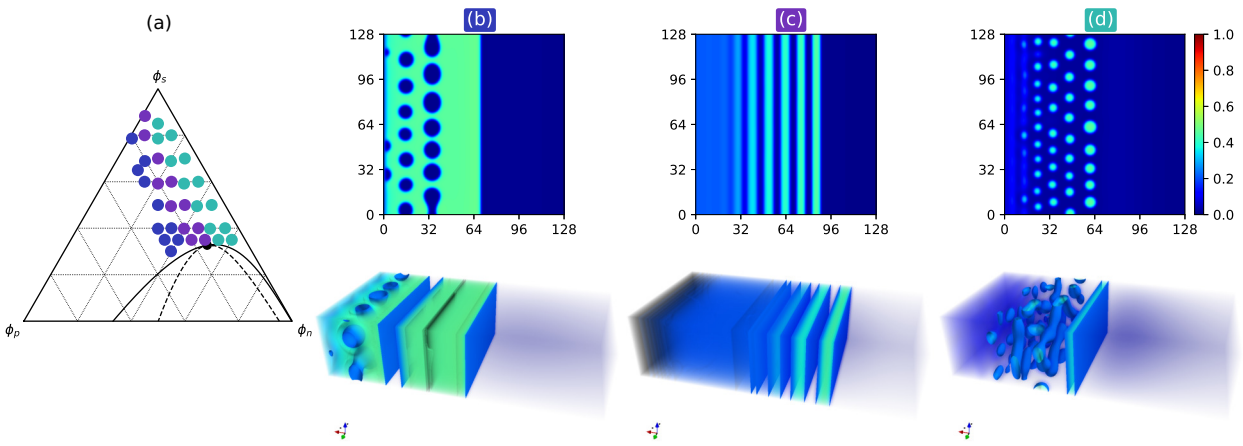

Figure 12: (a) Long-time simulations exhibiting late-time regime III colored by the observed microstructure in 2D simulations: non-solvent droplets in a polymer matrix (blue), alternating bands of polymer and nonsolvent (purple) and polymer droplets in nonsolvent (blue-green). 2D contour plots ($128R_0 \times 128R_0$) and 3D density plots ($128R_0 \times 64R_0 \times 32R_0$) of the polymer concentration showing microstructure: (b) nonsolvent droplets, (c) alternating bands and (d) polymer droplets. The color bar on the right of (d) indicates polymer concentration and is valid for both 2D and 3D plots.

code described here in simulations with both hydrodynamics and time-dependent boundary conditions.

In addition to the results related to film thickness, our model predicts three regimes of phase separation behavior at both early and late times: (I) a non-phase separating film/bath interface, (II) a phase separated film/bath interface and (III) a film that undergoes spinodal decomposition (Figures 5, 6, 9 and 10). At early times, certain film compositions undergo immediate spinodal decomposition, even though the initial film composition is not within the spinodal window. At late times, solvent and nonsolvent exchange drive a much larger set of film compositions into the spinodal envelope after a delay time.

We hypothesize that regime III at early and late times corresponds to the oft-observed phenomena of "instantaneous" and "delayed" precipitation in NIPS experiments.[1,5,6,28,30–32] As far as we know, ours are the first theoretical results predicting the existence of regime III in both early and late-time NIPS simulations.

Classic 1D transport models of membrane formation were able to distinguish between regimes that did not cross the binodal (approximately regime I) and regimes that did (approximately regimes II and III).[6,32] However, as our results show, the phase separation kinetics are more subtle than was previously assumed. In earlier models, researchers assumed that a system whose early-time composition path crossed into the binodal resulted in an instantaneous phase separation.[6] From Figure 5 it is clear that this assumption results in a much larger composition window for instantaneous precipitation than our model predicts.

Nevertheless, we state the important caveat that the present model does not include thermal fluctuations, and therefore cannot account for nucleation phenomena. If a quench is sufficiently deep so that the nucleation time is small relative to the nonsolvent diffusion time, the size of the composition window where phase separation can occur could be significantly larger. By contrast, shallow quenches with a large nucleation time will instead give rise to an additional mechanism for delayed precipitation.

Figure 9 shows how the delay time changes with the initial film composition and Figure S2 explores how the polymer/nonsolvent interaction parameter, nonsolvent/solvent in-

teraction parameter, and polymer molecular weight influence the phase separation behavior of the model. The model predicts that the delay time will increase with increasing polymer concentration and decreasing nonsolvent concentration in the initial film. Also, a less miscible solvent/nonsolvent pair shrinks the window for early-time spinodal decomposition and delays phase separation, while a larger polymer/nonsolvent interaction parameter (a deeper quench) increases the early-time spinodal window and speeds up phase separation.

While there is a large literature covering an array of polymer/solvent/nonsolvent systems, and exceptions can be found, these results qualitatively agree with experiment. For example, a classic review by Smolders examining macrovoid formation found that slower solvent/nonsolvent exchange accompanied an increase in the polymer concentration or decreased nonsolvent concentration in the film, and a lower miscibility of the solvent in the nonsolvent (higher χ_{ns}).[33] Similar results have been found in more recent literature,[3,28,29,34–38] with notable results by Hołda et al. who measure a linear increase in the delay time with increasing polymer concentration for polysulfone in N-methyl-2-pyrrolidone (NMP) and Tetrahydrofuran (THF).[36]

Fig 7 and Fig 12 show two and three dimensional morphologies obtained from short and long time simulations of the NIPS process. The film morphology is largely dictated by the polymer concentration. At low polymer concentration, the polymer microstructure consists of disconnected droplets and at higher concentration the polymer domains percolate and nonsolvent voids are formed. Phase separation proceeds as a surface-directed travelling wave, giving rise to a thin layer of polymer at the top of most films. We do not observe a qualitative difference in morphology between the early time and late time simulations, nor do we observe noticeably asymmetric domain sizes, except those produced by rapidly coarsening domains near the top of the film. We also observe film shrinking and swelling. As shown in Fig 11, the swelling ratio is a non-monotonic function of the polymer concentration, but shrinking is observed at low and intermediate polymer concentrations.

Other simulations of inhomogeneous ternary phase separations are largely in agreement with those presented here. Zhou and Powell observe a thin polymer layer at the top of phase-separating films using a phase-field model,[14] as does Akthakul et al. using a lattice Boltzmann model.[39] Recent DPD[40] and kinetic Monte Carlo[41,42] simulations are less systematic, but the morphologies in their simulations do not appear to show a layer and are clearly strongly influenced by thermal fluctuations.

Comparing to the experimental literature, it appears that our simulations (and all of the others of which we are aware) are still missing key pieces that are needed to fully explain experimental observations. We do not see important trends like a change in morphology based on fast or slow precipitation, nor do we observe the formation of macrovoids.[25]

Nevertheless, there is some promising agreement with qualitative trends. Our model predicts that films will shrink at intermediate polymer concentrations, which is repeatedly seen in experiment.[3] Also, it seems reasonable to hypothesize that the thin strip we observe at the top of our film may be one origin of the skin layer observed in many experiments.[31,33] However, many membranes are also made with an evaporation step prior to NIPS, and there is strong evidence that evaporation time is correlated with skin formation.[31,36]

More promising is the strong connection observed in experiments between the initial polymer concentration in the film and the final morphology.[3,28,29,35,38,43] For example, Zhang et al. observed that an increasing polymer concentration caused the morphology to transition from a more open finger-like structure to a more dense sponge-like structure, consistent with our simulation results.[38] Barth and coworkers have also claimed to see signatures of a change from spinodal decomposition to nucleation and growth kinetics using light scattering.[35]

Clearly, we still do not fully understand the NIPS mechanism and much work remains. We still do not have a definitive answer to the origin of skin layers, asymmetric vertical pore

size gradients or macrovoids. Two of the most important features that are missing from our model, nucleation and growth kinetics and solidification, are obvious frontiers for additional research. The fact that solidification plays an important role at a separate time scale is clear from experiments, which observe both a phase separating front and a "gelation" front in phase separating membranes.[28,30] Additional areas of investigation include the interaction between pre-evaporation steps and NIPS, the role of coarsening, the unique impacts of viscoelasticity, the effects of fluid inertia and non-vitreous solidification processes, such as crystallization. While these phenomena are accessible via two-fluid models, some will require additional physics and different numerical methods, which (especially in the case of viscoelasticity) will almost certainly increase computational cost.

Acknowledgement We would like to acknowledge financial support from Asahi Kasei Corporation, the MRSEC Program of the National Science Foundation through Grant No. DMR-1720256 (IRG-3), and from Brigham Young University. Additionally, we acknowledge computational resources from the BYU Office of Research Computing and from the Center for Scientific Computing from the CNSI, MRL: an NSF MRSEC (DMR-1720256) and NSF CNS-1725797.

References

(1) P. van de Witte, P. Dijkstra, J. van den Berg and J. Feijen, *J. Membr. Sci.*, 1996, **117**, 1–31.

(2) C. Sosa, R. Liu, C. Tang, F. Qu, S. Niu, M. Z. Bazant, R. K. Prudhomme and R. D. Priestley, *Macromolecules*, 2016, **49**, 3580–3585.

(3) C. E. Udoh, V. Garbin and J. T. Cabral, *Langmuir*, 2016, **32**, 8131–8140.

(4) A. J. Parnell, A. L. Washington, O. O. Mykhaylyk, C. J. Hill, A. Bianco, S. L. Burg, A. J. C. Dennison, M. Snape, A. J. Cadby, A. Smith and et al., *Sci. Rep.*, 2015, **5**, 18317.

(5) A. Reuvers and C. Smolders, *J. Membr. Sci.*, 1987, **34**, 67–86.

(6) C. S. Tsay and A. J. McHugh, *J. Polym. Sci. Pol. Phys.*, 1990, **28**, 1327–1365.

(7) L.-P. Cheng, Y. S. Soh, A.-H. Dwan and C. C. Gryte, *J. Polym. Sci., Part B: Polym. Phys.*, 1994, **32**, 1413–1425.

(8) B. F. Barton, P. D. Graham and A. J. McHugh, *Macromolecules*, 1998, **31**, 1672–1679.

(9) H. Chen and A. Chakrabarti, *J. Chem. Phys.*, 1998, **108**, 6006.

(10) A. Aksimentiev, K. Moorthi and R. Holyst, *J. Chem. Phys.*, 2000, **112**, 6049.

(11) R. A. L. Jones, L. J. Norton, E. J. Kramer, F. S. Bates and P. Wiltzius, *Phys. Rev. Lett.*, 1991, **66**, 1326–1329.

(12) R. C. Ball and R. L. H. Essery, *J. Phys.: Condens. Matter*, 1990, **2**, 10303–10320.

(13) N. S. Martys and J. F. Douglas, *Phys. Rev. E*, 2001, **63**, year.

(14) B. Zhou and A. C. Powell, *J. Membr. Sci.*, 2006, **268**, 150–164.

(15) D. R. Tree, K. T. Delaney, H. D. Ceniceros, T. Iwama and G. H. Fredrickson, *Soft Matter*, 2017, **13**, 3013–3030.

(16) M. R. Cervellere, Y. hui Tang, X. Qian, D. M. Ford and P. C. Millett, *J. Membr. Sci.*, 2019, **577**, 266–273.

(17) P. G. de Gennes, *J. Chem. Phys.*, 1980, **72**, 4756.

(18) M. Doi and A. Onuki, *J. Phys. II France*, 1992, **2**, 1631–1656.

(19) H. Tanaka, *J. Phys.-Condens. Mat.*, 2000, **12**, R207.

(20) I. Schmidt and K. Binder, *J. Phys.*, 1985, **46**, 1631–1644.

(21) S.-M. Hur, C. J. Garcia-Cervera and G. H. Fredrickson, *Macromolecules*, 2012, **45**, 2905–2919.

(22) R. L. Pego, *P. Roy. Soc. A-Math. Phy*, 1989, **422**, 261–278.

(23) D. A. Tarzia, *MAT-Serie A*, 2000, **2**, 1–297.

(24) J. F. Marko, *Phys. Rev. E*, 1993, **48**, 2861–2879.

(25) D. R. Tree, T. Iwama, K. T. Delaney, J. Lee and G. H. Fredrickson, *ACS Macro Lett.*, 2018, **7**, 582–586.

(26) S. P. Paradiso, K. T. Delaney, C. J. Garcia-Cervera, H. D. Ceniceros and G. H. Fredrickson, *Macromolecules*, 2016, **49**, 1743–1751.

(27) S. S. Prakash, L. F. Francis and L. E. Scriven, *J. Membr. Sci.*, 2008, **313**, 135–157.

(28) A. J. McHugh and C. S. Tsay, *J. Appl. Polym. Sci.*, 1992, **46**, 2011–2021.

(29) G. Gaides and A. McHugh, *J. Membr. Sci.*, 1992, **74**, 83–94.

(30) A. McHugh and D. Miller, *J. Membr. Sci.*, 1995, **105**, 121–136.

(31) H. Strathmann, K. Kock, P. Amar and R. Baker, *Desalination*, 1975, **16**, 179–203.

(32) A. J. Reuvers, J. W. A. van den Berg and C. A. Smolders, *J. Membr. Sci.*, 1987, **34**, 45–65.

(33) C. A. Smolders, A. J. Reuvers, R. M. Boom and I. M. Wienk, *J. Membr. Sci.*, 1992, **73**, 259–275.

(34) T. D. Nguyen, T. Matsuura and S. Sourirajan, *Chem. Eng. Commun.*, 1987, **57**, 351–369.

(35) C. Barth, M. Gonalves, A. Pires, J. Roeder and B. Wolf, *J. Membr. Sci.*, 2000, **169**, 287–299.

(36) A. K. Hołda, B. Aernouts, W. Saeys and I. F. Vankelecom, *J. Membr. Sci.*, 2013, **442**, 196–205.

(37) G. R. Guillen, G. Z. Ramon, H. P. Kavehpour, R. B. Kaner and E. M. Hoek, *J. Membr. Sci.*, 2013, **431**, 212–220.

(38) Q. Zhang, Y. M. Li, Y. Gu, R. M. Dorin and U. Wiesner, *Polymer*, 2016, **107**, 398–405.

(39) A. Akthakul, C. E. Scott, A. M. Mayes and A. J. Wagner, *J. Membr. Sci.*, 2005, **249**, 213–226.

(40) X.-L. Wang, H.-J. Qian, L.-J. Chen, Z.-Y. Lu and Z.-S. Li, *J. Membr. Sci.*, 2008, **311**, 251–258.

(41) Y. Termonia, *Phys. Rev. Lett.*, 1994, **72**, 3678–3681.

(42) X. He, C. Chen, Z. Jiang and Y. Su, *J. Membr. Sci.*, 2011, **371**, 108–116.

(43) Y. Su, C. Kuo, D. Wang, J. Lai, A. Deratani, C. Pochat and D. Bouyer, *J. Membr. Sci.*, 2009, **338**, 17–28.

Supporting Information: Mass-transfer driven spinodal decomposition in a ternary polymer solution

Douglas R. Tree,[†] Lucas Francisco Dos Santos ,[‡] Jan U. Garcia,[¶] Caden B. Wilson,[†] Timothy R. Scott,[†] and Glenn H. Fredrickson[*,§,‖,¶]

[†]*Chemical Engineering Department, Brigham Young University, Provo, Utah*

[‡]*Universidade Estadual de Maringá, Maringá, Paraná, Brazil*

[¶]*Chemical Engineering Department, University of California, Santa Barbara*

[§]*Materials Research Laboratory, University of California, Santa Barbara*

[‖]*Materials Department, University of California, Santa Barbara*

E-mail: tree.doug@byu.edu

Hybrid Pseudo-Spectral/Finite-Difference Method

In a previous paper,[S1] several of us outlined a method for solving the multi-fluid model represented by Equations 1–3 in the main text using pseudo-spectral methods and a semi-implicit time discretization scheme. The combination of accuracy and stability provided by these methods allows one to efficiently solve the multi-fluid model equations in spite of the inherent disparity of length and time scales in the model.

The choice of a pseudo-spectral (PS) spatial discretization was key to the previous method's success. As mentioned, PS methods give unparalleled accuracy, and Fourier transforms result in diagonal terms for linear differential operators, allowing a facile solution to

the semi-implicit schemes that stabilize the time integration.[S1] Unfortunately, PS methods are limited to periodic boundary conditions (with a full Fourier transform) or homogeneous Dirichlet/Neumann conditions (with sine/cosine transforms), neither of which is sufficient to model a large nonsolvent bath.[S2]

Alternatively, finite difference (FD) methods provide ample flexibility in treating boundary conditions, but are considerably less accurate than PS schemes. Worse still, a multi-dimensional FD discretization results in a large, sparse matrix that is costly to invert when time-stepping with a semi-implicit method.

In an attempt to capture the major benefits of both approaches, we present here a hybrid PS/FD spatial discretization scheme where one dimension is treated via finite differences, and the remaining dimensions are discretized pseudo-spectrally. The single FD dimension is able to provide time-dependent, inhomogeneous boundary conditions that are flexible enough to simulate the nonsolvent bath. Additionally, this one-dimensional discretization gives a banded matrix that can be cheaply inverted in semi-implicit schemes.

Accordingly, numerical methods to solve both the convection-diffusion equation and the momentum equations (Eqs. 1–3) using a hybrid PS/FD scheme to discretize space are described below.

Diffusion Equation

It is convenient to examine the convection-diffusion equation, Eq. 1, written explicitly in terms of the volume fractions, ϕ_i. To do so, we define diffusivity and gradient coefficient matrices,

$$D_{ij} = \sum_k M_{ik} H_{kj} \tag{1}$$

$$B_{ij} = \sum_k M_{ik} K_{kj} \tag{2}$$

where M_{ij} is the mobility matrix, H_{ij} is the Hessian matrix of second derivatives of the free energy functional and K_{ij} is a diagonal matrix of the gradient coefficients.[S1] Substituting these definitions into Eq. 1 in the main text yields,

$$\frac{\partial \phi_i}{\partial t} + \boldsymbol{v} \cdot \nabla \phi_i = \nabla \cdot \left[\sum_j^{p,n} \left(D_{ij} \nabla \phi_j - B_{ij} \nabla \nabla^2 \phi_j \right) \right] \tag{3}$$

To integrate Eq. 3 we need a method for the time integration in addition to a discretization of the spatial derivatives. We approximate the time derivative via a semi-implicit method. We begin by re-arranging Eq. 3 to a more useful form. Positive and negative linear terms are introduced on the right-hand side giving,

$$\begin{aligned} \frac{\partial \phi_i}{\partial t} + \boldsymbol{v} \cdot \nabla \phi_i =& \nabla \cdot (D_{ij} \nabla \phi_j) + D^*_{ij} \nabla^2 \phi_j - D^*_{ij} \nabla^2 \phi_j \\ & - \nabla \cdot \left(B_{ij} \nabla \nabla^2 \phi_j \right) + B^*_{ij} \nabla^4 \phi_j - B^*_{ij} \nabla^4 \phi_j . \end{aligned} \tag{4}$$

Here, D^*_{ij} and B^*_{ij} are arbitrary constant matrices[1], and summation over repeated indices has been assumed in order to avoid cumbersome summation symbols. Defining $\delta D_{ij} \equiv D_{ij} - D^*_{ij}$ and $\delta B_{ij} \equiv B_{ij} - B^*_{ij}$ as the difference between the concentration-dependent coefficient matrices and our chosen constant matrices, Eq. 4 becomes,

$$\frac{\partial \phi_i}{\partial t} + \boldsymbol{v} \cdot \nabla \phi_i = \nabla \cdot (\delta D_{ij} \nabla \phi_j) + D^*_{ij} \nabla^2 \phi_j - \nabla \cdot \left(\delta B_{ij} \nabla \nabla^2 \phi_j \right) - B^*_{ij} \nabla^4 \phi_j \tag{5}$$

Finally, time is discretized with the non-linear terms being treated explicitly and the linear terms being treated implicitly. Doing so gives,

$$\frac{\phi_i^{n+1} - \phi_i^n}{\Delta t} + \boldsymbol{v}^n \cdot \nabla \phi_i^n = \nabla \cdot \left(\delta D_{ij}^n \nabla \phi_j^n \right) + D^*_{ij} \nabla^2 \phi_j^{n+1} - \nabla \cdot \left(\delta B_{ij}^n \nabla \nabla^2 \phi_j^n \right) - B^*_{ij} \nabla^4 \phi_j^{n+1} \tag{6}$$

which completes the semi-implicit time-stepping scheme.

[1] In our previous work,[S1] we found that a prudent choice of D^*_{ij} and B^*_{ij} led to an unconditionally stable time integration. Specifically, both matrices has to be (i) positive definite and (ii) have an eigenvalue at least as large as the largest eigenvalue in $D_{ij}(\phi_p, \phi_n)$ or $B_{ij}(\phi_p, \phi_n)$ respectively.

To compute ϕ_i^{n+1} in Eq. 6, the spatial derivatives must be discretized. In our previous work, we approximated these derivatives using numerical Fourier transforms on a collocated grid, i.e. a pseudo-spectral approximation.[S1,S3] Presently, we will discretize the x-axis via finite differences and the y and z dimensions pseudo-spectrally. Note that the choice of which dimension to treat via FD is arbitrary, so we can choose x as the FD dimension without a loss of generality.

First, we discretize the implicit terms to isolate ϕ_i^{n+1}. These terms contain second- and fourth-order gradient operators, which when separating the x derivatives from the y and z derivatives are given by,

$$\nabla^2\phi_j = \frac{\partial^2\phi_j}{\partial x^2} + \nabla_{yz}^2\phi_j \tag{7}$$

$$\nabla^4\phi_j = \frac{\partial^4\phi_j}{\partial x^4} + 2\frac{\partial^2}{\partial x^2}\nabla_{yz}^2\phi_j + \nabla_{yz}^4\phi_j \tag{8}$$

where

$$\nabla_{yz} = \left(\frac{\partial\phi_j}{\partial y}, \frac{\partial\phi_j}{\partial z}\right)^{\mathrm{T}} \tag{9}$$

is a two-dimensional gradient for the PS directions only. Applying a yz-Fourier transform to the operators gives,

$$\mathcal{F}_{yz}[\nabla^2\phi_j] = \frac{\partial^2\hat{\phi}_j}{\partial x^2} - q^2\hat{\phi}_j \tag{10}$$

$$\mathcal{F}_{yz}[\nabla^4\phi_j] = \frac{\partial^4\hat{\phi}_j}{\partial x^4} - 2q^2\frac{\partial^2\hat{\phi}_j}{\partial x^2} + q^4\hat{\phi}_j \tag{11}$$

where the wavevector $\boldsymbol{q} = (q_y, q_z)^T$, $q = |\boldsymbol{q}|$ and $\hat{\phi}_j = \mathcal{F}_{yz}[\phi_j]$.

With these expressions in hand, we now take the Fourier transform of Eq. 6, and substi-

tute Eq. 10 and Eq. 11 where appropriate. This gives,

$$\frac{\hat{\phi}_i^{n+1} - \hat{\phi}_i^n}{\Delta t} + \mathcal{F}_{yz}\left[\boldsymbol{v}^n \cdot \nabla \phi_i^n\right] = \mathcal{F}_{yz}\left[\nabla \cdot \left(\delta D_{ij}^n \nabla \phi_j^n\right)\right] - \mathcal{F}_{yz}\left[\nabla \cdot \left(\delta B_{ij}^n \nabla \nabla^2 \phi_j^n\right)\right] + D_{ij}^* \left(\frac{\partial^2 \hat{\phi}_j^{n+1}}{\partial x^2} - q^2 \hat{\phi}_j^{n+1}\right) - B_{ij}^* \left(\frac{\partial^4 \hat{\phi}_j^{n+1}}{\partial x^4} - 2q^2 \frac{\partial^2 \hat{\phi}_j^{n+1}}{\partial x^2} + q^4 \hat{\phi}_j^{n+1}\right) \quad (12)$$

which upon solving for $\hat{\phi}_j^{n+1}$ yields,

$$\left[I_{ij} - \Delta t D_{ij}^* \left(\frac{\partial^2}{\partial x^2} - q^2\right) + \Delta t B_{ij}^* \left(\frac{\partial^4}{\partial x^4} - 2q^2 \frac{\partial^2}{\partial x^2} + q^4\right)\right] \hat{\phi}_j^{n+1} = \hat{\phi}_i^n - \Delta t \mathcal{F}_{yz}\left[\boldsymbol{v}^n \cdot \nabla \phi_i^n + \nabla \cdot \left(\delta D_{ij}^n \nabla \phi_j^n\right) - \nabla \cdot \left(\delta B_{ij}^n \nabla \nabla^2 \phi_j^n\right)\right]. \quad (13)$$

To evaluate the x-derivatives on the left-hand side of Eq. 13, the x-direction is discretized into a regular grid with M points and spacing Δx. Finite difference formulas[S4] are then substituted for the x-derivatives into Eq. 13. For example, centered, second-order finite difference formulas for an interior node at $x = x_m$ are given by,

$$\frac{\partial^2 \hat{\phi}_{j,m}^{n+1}}{\partial x^2} \approx \frac{\hat{\phi}_{j,m+1}^{n+1} - 2\hat{\phi}_{j,m}^{n+1} + \hat{\phi}_{j,m-1}^{n+1}}{\Delta x^2} \quad (14)$$

$$\frac{\partial^4 \hat{\phi}_{j,m}^{n+1}}{\partial x^4} \approx \frac{\hat{\phi}_{j,m+2}^{n+1} - 4\hat{\phi}_{j,m+1}^{n+1} + 6\hat{\phi}_{j,m}^{n+1} - 4\hat{\phi}_{j,m-1}^{n+1} + \hat{\phi}_{j,m-2}^{n+1}}{\Delta x^4} \quad (15)$$

where the subscript j indicates the component, the subscript m indicates the node and the superscript $n+1$ indicates the time point. More details about boundary conditions and the attendant complications of the treatment of the end nodes via finite differences can be found below.

Upon substitution of the FD formulas, Eq. 13 is of the form

$$\boldsymbol{A}_{ij} \hat{\phi}_j^{n+1} = \boldsymbol{b}_i \quad (16)$$

where

$$\boldsymbol{A}_{ij} = \left[I_{ij} - \Delta t D^*_{ij} \left(\frac{\partial^2}{\partial x^2} - q^2 \right) + \Delta t B^*_{ij} \left(\frac{\partial^4}{\partial x^4} - 2q^2 \frac{\partial^2}{\partial x^2} + q^4 \right) \right] \tag{17}$$

is a square $\mathcal{M} \times \mathcal{M}$ block-banded matrix where $\mathcal{M} = NM$ with N being the number of components and M (as defined above) is the number of grid points spanning the x direction. The right hand side is the $\mathcal{M} \times 1$ nonlinear vector function,

$$\boldsymbol{b}_i = f(\hat{\phi}^n_i) = \hat{\phi}^n_i - \Delta t \mathcal{F}_{yz} \left[\boldsymbol{v}^n \cdot \nabla \phi^n_i + \nabla \cdot \left(\delta D^n_{ij} \nabla \phi^n_j \right) - \nabla \cdot \left(\delta B^n_{ij} \nabla \nabla^2 \phi^n_j \right) \right]. \tag{18}$$

The right-hand side vector, Eq. 18, can be evaluated at each FD node using a combination of forward and inverse fast-Fourier transforms and finite difference formulas using the known quanitity ϕ^n_j. For example, the second-order gradient can be decomposed into FD and PS derivatives,

$$\nabla \cdot (\delta D^n_{ij} \nabla \phi^n_j) = \frac{\partial}{\partial x} \left(\delta D^n_{ij} \frac{\partial \phi^n_j}{\partial x} \right) + \nabla_{yz} \cdot (\delta D^n_{ij} \nabla_{yz} \phi^n_j). \tag{19}$$

Because of the non-constant coefficients δD^n_{ij} and δB^n_{ij}, care must be taken to use self-adjoint finite difference operators for the x-derivative on the right-hand side of Eq. 19.[S5] In this case, the recursive, second-order, self-adjoint, centered finite difference formula

$$\frac{df_m}{dx} = \frac{f_{m+1/2} - f_{m-1/2}}{\Delta x} + \mathrm{O}(\Delta x^2) \tag{20}$$

results in

$$\frac{\partial}{\partial x} \left(\delta D^n_{ij,\,m} \frac{\partial \phi^n_j}{\partial x} \right) = \frac{\delta D^n_{ij,\,m+\frac{1}{2}} (\phi^n_{j,m+1} - \phi^n_{j,m}) - \delta D^n_{ij,m-\frac{1}{2}} (\phi^n_{j,m} - \phi^n_{j,m-1})}{\Delta x^2}. \tag{21}$$

for each node m, where $\delta D^n_{ij,\,m+\frac{1}{2}}$ and $\delta D^n_{ij,m-\frac{1}{2}}$ can be obtained via linear interpolation. The second term on the right-hand side of Eq. 19 can be evaluated using repeated forward and

inverse Fourier transforms, for example,

$$\mathcal{F}_{yz}[\nabla_{yz} \cdot (\delta D_{ij}^n \nabla_{yz} \phi_j^n)] = i\boldsymbol{q} \cdot \mathcal{F}_{yz} \left[\delta D_{ij}^n \mathcal{F}_{yz}^{-1}[i\boldsymbol{q}\hat{\phi}_j^n] \right]. \tag{22}$$

The method for evaluating the fourth-order gradient term and the edge nodes is similar to the example shown here, noting that self-adjoint finite difference formulas are needed in both cases.

Finally, once $\boldsymbol{A}_{ij}$ and $\boldsymbol{b}_i$ have been calculated (including the boundary conditions), the linear equation (Eq. 16) can be solved. Because $\boldsymbol{A}_{ij}$ is banded, it can be efficiently solved in $\mathrm{O}(\mathcal{M})$ time, which was one of the primary motivating factors for using a hybrid FD/PS method from the outset.

Momentum Equation

The main difficulty in solving the momentum equation (Eq. 2 in the main text) is (i) satisfying Eq. 3, the incompressibility constraint, and (ii) efficiently dealing with a concentration-dependent viscosity. In our previous PS-only method,[S1] (i) was accomplished by eliminating the incompressibility constraint via the transverse projection operator, which can be explicitly written in terms of the wavevector $\boldsymbol{q}$ in Fourier space. Difficulty (ii) was overcome by using an iterative Picard's method modified with a first-order continuation guess and Anderson mixing to accelerate convergence.

Moving to a hybrid FD/PS method, the transverse projection operator is no longer a viable option for satisfying incompressibility. Instead, we derive a so-called "pressure–Poisson" equation[S6] that allows explicit access to the pressure and a subsequent solution to Eq. 2. Fortunately, Picard's method (accompanied by continuation and Anderson mixing) is still an effective method for dealing with a concentration-dependent viscosity.

Anticipating the need to formally solve for $\boldsymbol{v}$ for a future Picard iteration, the first step in the derivation of the numerical method involves the addition and subtraction of a linear

viscous dissipation term to Eq. 2,

$$0 = -\nabla p - \nabla \cdot \mathbf{\Pi} + \nabla \cdot \left[\eta(\nabla \boldsymbol{v} + \nabla \boldsymbol{v}^T)\right] + \eta^* \nabla^2 \boldsymbol{v} - \eta^* \nabla^2 \boldsymbol{v} \tag{23}$$

where η^* is an arbitrary constant[2] chosen for stability in the Picard iteration. For convenience, we define an excess stress tensor as the viscous stress due to the local difference in viscosity from η^*,

$$\boldsymbol{\sigma}_{\text{ex}} \equiv (\eta - \eta^*)(\nabla \boldsymbol{v} + \nabla \boldsymbol{v}^T) \tag{24}$$

which upon substitution into Eq. 23 and re-arrangement gives,

$$\eta^* \nabla^2 \boldsymbol{v} = \nabla \cdot (p\boldsymbol{I} + \mathbf{\Pi} - \boldsymbol{\sigma}_{\text{ex}}) \tag{25}$$

By taking the divergence of Eq. 25, one obtains a pressure-Poisson equation

$$\nabla^2 p = \nabla\nabla : (\boldsymbol{\sigma}_{\text{ex}} - \mathbf{\Pi}) \tag{26}$$

noting that the term on the left-hand side is eliminated using incompressibility, $\nabla \cdot \boldsymbol{v} = 0$.

Equations 24–26 represent a complete statement of momentum conservation and incompressibility, and can be used to solve for the velocity at a given time[3]. This is done by discretizing the gradient operators and formally solving for p and $\boldsymbol{v}$ (remember that $\boldsymbol{\sigma}_{\text{ex}}$ depends on $\boldsymbol{v}$). Both Eqs. 25 and 26 contain the Laplacian operator, which is given in Eq. 10 above. Expanding the Laplacian operators on the left-hand side and taking a yz-Fourier

[2]Our numerical testing indicates that choosing $\eta^* = \max(\eta)$ results in an unconditionally stable iteration.

[3]Note that unlike the diffusion equation, no time derivative appears in Equations 24–26. Instead, the time-dependence is implicit through the appearance of the volume-fraction in the osmotic stress and viscosity.

transform gives,

$$\left(\frac{\partial^2}{\partial x^2} - q^2\right)\hat{p} = \mathcal{F}_{yz}\left[\nabla\nabla : (\boldsymbol{\sigma}_{\text{ex}} - \boldsymbol{\Pi})\right] \tag{27}$$

$$\left(\frac{\partial^2}{\partial x^2} - q^2\right)\hat{\boldsymbol{v}} = \frac{1}{\eta^*}\mathcal{F}_{yz}\left[\nabla \cdot (p\boldsymbol{I} + \boldsymbol{\Pi} - \boldsymbol{\sigma}_{\text{ex}})\right] \tag{28}$$

Using the finite difference formula in Eq. 14 for the x-derivatives, these discretized equations reduce to a system of nonlinear equations of the form,

$$\boldsymbol{B}\hat{p} = g(\hat{\phi}_i^{n+1}, \hat{\boldsymbol{v}}) \tag{29}$$

$$\boldsymbol{C}\hat{\boldsymbol{v}} = \boldsymbol{h}(\hat{\phi}_i^{n+1}, \hat{\boldsymbol{v}}, \hat{p}) \tag{30}$$

where $\boldsymbol{B}$ is an $M \times M$ banded matrix and $\boldsymbol{C}$ is a $3M \times 3M$ banded matrix. Because both matrices are banded, they can be solved in $\mathrm{O}(M)$ time.

The coupled set of equations are iteratively solved using Picard's method,

$$\boldsymbol{B}\hat{p}^{k+1} = g(\hat{\phi}_i^{n+1}, \hat{\boldsymbol{v}}^k) \tag{31}$$

$$\boldsymbol{C}\hat{\boldsymbol{v}}^{k+1} = \boldsymbol{h}(\hat{\phi}_i^{n+1}, \hat{\boldsymbol{v}}^k, \hat{p}^k) \tag{32}$$

where k denotes the iterative index. The method proceeds as follows:

1. The divergence of the osmotic stress tensor, $\nabla\cdot\boldsymbol{\Pi}$ (Eq. 8 in the main text), is calculated using the volume fractions obtained from the diffusion equation, ϕ_i^{n+1}.

2. A velocity guess, $\boldsymbol{v}^k$ is obtained from a continuation method based on the velocities at previous timesteps, $\boldsymbol{v}^n$, $\boldsymbol{v}^{n-1}$, ..., or previous iterations $\boldsymbol{v}^k$, $\boldsymbol{v}^{k-1}$, ..., and is used to calculate the divergence of the excess viscous stress, $\nabla \cdot \boldsymbol{\sigma}_{\text{ex}}$.

3. $\nabla\cdot\boldsymbol{\Pi}$ and $\nabla\cdot\boldsymbol{\sigma}_{\text{ex}}$ are used to evaluate the right-hand side of Eq. 31, and the (now-linear) system is solved for the pressure p^{k+1}.

4. The right-hand side of Eq. 32 is evaluated, and the linear system is solved for a new velocity, $\boldsymbol{v}^{k+1}$.

5. The norm of the difference between velocity vectors, $|\boldsymbol{v}^{k+1} - \boldsymbol{v}^{k}|$ is compared to a specified tolerance (in our case, typically 10^{-6}). If the norm is small enough, the iteration terminates. If not, one returns to step two[4] and performs another iteration.

Finally, for completeness, we provide some details regarding the evaluation of the functions,

$$g(\hat{\phi}_i^{n+1}, \hat{\boldsymbol{v}}^k) = \mathcal{F}_{yz}\left[\nabla\nabla : (\boldsymbol{\sigma}_{\text{ex}} - \boldsymbol{\Pi})\right] \tag{33}$$

$$\boldsymbol{h}(\hat{\phi}_i^{n+1}, \hat{\boldsymbol{v}}^k, \hat{p}^k) = \frac{1}{\eta^*}\mathcal{F}_{yz}\left[\nabla \cdot (p\boldsymbol{I} + \boldsymbol{\Pi} - \boldsymbol{\sigma}_{\text{ex}})\right] \tag{34}$$

from the right-hand sides of Eqs. 31 and 32. For the most part, this process is straightforward, and these functions are evaluated using principles similar to those discussed for the diffusion equation. Namely, one must use (i) self-adjoint finite difference operators for the x-derivatives and (ii) repeated forward and reverse yz-Fourier transforms for the y and z derivatives.

However, the expansion of the derivative operators in Eqs. 33 and 34 is more complex than those on the right-hand side of the diffusion equation, so we document them here. Expanding the terms in g gives,

$$\nabla\nabla : \boldsymbol{\sigma}_{\text{ex}} = \nabla\nabla : (\delta\eta\nabla\boldsymbol{v}) + \nabla\nabla : (\delta\eta(\nabla\boldsymbol{v})^T) \tag{35}$$

$$\begin{aligned} &= 2\frac{\partial^2}{\partial x^2}\left(\delta\eta\frac{\partial v_x}{\partial x}\right) + 2\nabla_{yz}\cdot\frac{\partial}{\partial x}\left(\delta\eta\frac{\partial \boldsymbol{v}_{yz}}{\partial x}\right) \\ &\quad + 2\nabla_{yz}\cdot\frac{\partial}{\partial x}\left(\delta\eta\nabla_{yz}v_x\right) + \nabla_{yz}\nabla_{yz} : \left(\delta\eta\nabla_{yz}\boldsymbol{v}_{yz}\right), \end{aligned} \tag{36}$$

[4]The osmotic stress tensor is not a function of $\boldsymbol{v}$ or p and therefore only needs to be calculated once.

and

$$\nabla\nabla : \mathbf{\Pi} = \nabla \cdot (\phi_i H_{ij} \nabla \phi_j) - \nabla \cdot \left(\phi_i K_{ij} \nabla \nabla^2 \phi_j\right) \tag{37}$$

$$\begin{aligned} &= \frac{\partial}{\partial x}\left(\phi_i H_{ij} \frac{\partial \phi_j}{\partial x}\right) + \nabla_{yz} \cdot (\phi_i H_{ij} \nabla_{yz} \phi_j) \\ &\quad - \frac{\partial}{\partial x}\left(\phi_i K_{ij} \frac{\partial^3 \phi_j}{\partial x^3}\right) - \frac{\partial}{\partial x}\left(\phi_i K_{ij} \frac{\partial}{\partial x} \nabla_{yz}^2 \phi_j\right) \\ &\quad - \nabla_{yz} \cdot \left(\phi_i K_{ij} \nabla_{yz} \frac{\partial^2 \phi_j}{\partial x^2}\right) - \nabla_{yz} \cdot \left(\phi_i K_{ij} \nabla_{yz} \nabla_{yz}^2 \phi_j\right). \end{aligned} \tag{38}$$

where $\delta\eta = \eta - \eta^*$ and $\boldsymbol{v}_{yz} = (v_y, v_z)^T$. Expanding the terms in $\boldsymbol{h}$ gives,

$$\nabla p = \left(\frac{\partial p}{\partial x}, \nabla_{yz} p\right)^T \tag{39}$$

$$\nabla \cdot \mathbf{\Pi} = \phi_i H_{ij} \nabla \phi_j - \phi_i K_{ij} \nabla \nabla^2 \phi_j \tag{40}$$

$$\begin{aligned} &= \left(\phi_i H_{ij} \frac{\partial \phi_j}{\partial x} - \phi_i K_{ij} \frac{\partial^3 \phi_j}{\partial x^3} - \phi_i K_{ij} \nabla_{yz}^2 \frac{\partial \phi_j}{\partial x}, \right. \\ &\qquad \left. \phi_i H_{ij} \nabla_{yz} \phi_j - \phi_i K_{ij} \nabla_{yz} \frac{\partial^2 \phi_j}{\partial x^2} - \phi_i K_{ij} \nabla_{yz} \nabla_{yz}^2 \phi_j\right)^T \end{aligned} \tag{41}$$

and

$$\nabla \cdot \boldsymbol{\sigma}_{\text{ex}} = \nabla \cdot [\delta\eta(\nabla \boldsymbol{v} + \nabla \boldsymbol{v}^T)] \tag{42}$$

$$\begin{aligned} &= \left(2\frac{\partial}{\partial x}(\delta\eta \frac{\partial v_x}{\partial x}) + \nabla_{yz} \cdot (\delta\eta \frac{\partial \boldsymbol{v}_{yz}}{\partial x}) + \nabla_{yz} \cdot (\delta\eta \nabla_{yz} v_x), \right. \\ &\qquad \left. \frac{\partial}{\partial x}(\delta\eta \frac{\partial \boldsymbol{v}_{yz}}{\partial x}) + \frac{\partial}{\partial x}\left(\delta\eta \nabla_{yz} v_x\right) + \nabla_{yz} \cdot [\delta\eta(\nabla_{yz} \boldsymbol{v}_{yz} + \nabla_{yz} \boldsymbol{v}_{yz}^T)]\right)^T, \end{aligned} \tag{43}$$

Numerically evaluating these expressions involves the use of both traditional and self-adjoint finite differences to approximate the x-derivatives, and repeated forward and inverse

yz-Fourier transforms where

$$\mathcal{F}_{yz}[\nabla_{yz}] = (iq_y, iq_z)^T \tag{44}$$

$$\mathcal{F}_{yz}[\nabla_{yz}\nabla_{yz}] = \begin{pmatrix} -q_y^2 & -q_y q_z \\ -q_y q_z & -q_z^2 \end{pmatrix} \tag{45}$$

are the pseudo-spectral yz-gradient operators. Finally, note that it is often convenient to exchange the order of operations between the Fourier transforms, x-derivatives and yz-derivatives, which is permitted since all are linear operators.

Boundary Conditions

As desired, the hybrid FD/PS method allows the implementation of boundary conditions for both the diffusion and momentum equations. For the thin-film geometry, the diffusion equation has two boundary conditions at each boundary (wall and bath). At the wall, we have a mass-conserving, no-flux condition

$$M_{ij} \left.\frac{d\mu_i}{dx}\right|_{x=\text{wall}} = 0, \tag{46}$$

and a prescription of the local contact angle

$$\left.\frac{d\phi_i}{dx}\right|_{x=\text{wall}} = -\frac{\chi_{wi}}{\kappa} \tag{47}$$

where χ_{wi} is the interaction coefficient between component i and the wall. The conditions in the bath are given by

$$\lim_{x\to\infty} \phi_i = \phi_i^{\text{b}} \tag{48}$$

$$\lim_{x\to\infty} \frac{d\phi_i}{dx} = 0. \tag{49}$$

For the momentum equation, we have boundary conditions for the velocity only.[S6] At the wall, we have the customary no-slip and no-penetration conditions, $\boldsymbol{v} = 0$. At the edge of the bath, we also require $\boldsymbol{v} = 0$, meaning the bath must still be large enough for all of the relevant hydrodynamics to decay to zero before reaching the bath "boundary." Future work with these methods could go further to implement "open" boundary conditions obviating the need for such a requirement.

In theory it is possible for a simulation of the thin film geometry with the above boundary conditions to have a $2\times$ speedup over an identical simulation using periodic conditions, due to a reduction in the needed domain size. However, in practice we find that finite difference derivatives require greater resolution than pseudospectral derivatives, eliminating the potential benefit. We also found that our PS code design was inherently faster, due to the relative easy and relatively low complexity compared to the hybrid FD/PS code. As such, all of the simulations of the thin film geometry in the present work were performed with the PS method.

However, long-time simulations require time-dependent boundary conditions, which can only be achieved via the hybrid FD/PS code. In these calculations, a 1D periodic simulation is first performed with a very large bath (typically $Lx = 4092\,R_0$). Two "boundaries" are then chosen: the axis of symmetry (the wall) and a point in the bath near to the eventual interface between the film and bath. The latter (x_{bath}) is chosen by convenience to be far away from the phase separating interface, but small enough to lead to a significant reduction in run-time. To verify that the choice of x_{bath} did not result in significant errors, concentrations from large-bath 1D simulations were compared to concentrations of 1D projections from the higher dimensional simulations.

At these boundaries, we proscribe,

$$\phi_i^{\mathrm{2D}}(x_{\mathrm{wall}}, t) = \phi_i^{\mathrm{1D}}(x_{wall}, t) \tag{50}$$

$$\left.\frac{d\phi_i^{\mathrm{2D}}(x,t)}{dx}\right|_{x=x_{\mathrm{wall}}} = \left.\frac{d\phi_i^{\mathrm{1D}}(x,t)}{dx}\right|_{x=x_{wall}} \tag{51}$$

$$\phi_i^{\mathrm{2D}}(x_{\mathrm{bath}}, t) = \phi_i^{\mathrm{1D}}(x_{\mathrm{bath}}, t) \tag{52}$$

$$\left.\frac{d\phi_i^{\mathrm{2D}}(x,t)}{dx}\right|_{x=x_{\mathrm{bath}}} = \left.\frac{d\phi_i^{\mathrm{1D}}(x,t)}{dx}\right|_{x=x_{\mathrm{bath}}} \tag{53}$$

for the volume fractions and

$$\boldsymbol{v}(x_{\mathrm{wall}}, t) = 0 \tag{54}$$

$$\boldsymbol{v}(x_{\mathrm{bath}}, t) = 0 \tag{55}$$

for the velocities. Again, when resolving hydrodynamics we require that the boundary be sufficiently far from the interface, so the velocity decays to zero to avoid an unphysical condition.

At the root of the hybrid FD/PS method, both the diffusion equation, Eq. 16, and the momentum equation, Eq. 32 are block-diagonal, linear matrix equations. Boundary conditions can be added by altering the elements of the matrix which correspond to the boundary grid point. We use straightforward finite difference techniques to discretize these boundary conditions.

For periodic boundary conditions, we use centered finite differences for all derivatives,

$$\left.\frac{df}{dx}\right|_{x_m} = \frac{f_{m+1} - f_{m-1}}{2\Delta x} \tag{56}$$

$$\left.\frac{d^2f}{dx^2}\right|_{x_m} = \frac{f_{m+1} - 2f_m + f_{m-1}}{(\Delta x)^2} \tag{57}$$

$$\left.\frac{d^3f}{dx^3}\right|_{x_m} = \frac{f_{m+2} - 2f_{m+1} + 2f_{m-1} - f_{m-2}}{2(\Delta x)^3} \tag{58}$$

$$\left.\frac{d^4f}{dx^4}\right|_{x_m} = \frac{f_{m+2} - 4f_{m+1} + 6f_m - 4f_{m-1} + f_{m-2}}{(\Delta x)^4} \tag{59}$$

where x_m is the location of the gridpoint in the x-direction. As is standard, calls to off-grid locations are "wrapped around" the boundary. For example if $i = 0$ on a grid with an upper limit of $N_x - 1$ points, then the finite difference formula for the third derivative would be,

$$\left.\frac{d^3f}{dx^3}\right|_{x_0} = \frac{f_2 - 2f_1 + 2f_{Nx-2} - f_{Nx-3}}{2(\Delta x)^3}. \tag{60}$$

For non-periodic boundary conditions, we use one-sided finite differences.[S4] On the left-side boundary we use,

$$\left.\frac{df}{dx}\right|_{x_m} = \frac{-\frac{1}{2}f_{m+2} + 2f_{m+1} - \frac{3}{2}f_m}{\Delta x} \tag{61}$$

$$\left.\frac{d^2f}{dx^2}\right|_{x_m} = \frac{-f_{m+3} + 4f_{m+2} - 5f_{m+1} + 2f_m}{(\Delta x)^2} \tag{62}$$

$$\left.\frac{d^3f}{dx^3}\right|_{x_m} = \frac{-\frac{3}{2}f_{m+4} + 7f_{m+3} - 12f_{m+2} + 9f_{m+1} - \frac{5}{2}f_m}{(\Delta x)^3} \tag{63}$$

$$\left.\frac{d^4f}{dx^4}\right|_{x_m} = \frac{-2f_{m+5} + 11f_{m+4} - 24f_{m+3} + 26f_{m+2} - 14f_{m+1} + 3f_m}{(\Delta x)^4} \tag{64}$$

and on the right-side we use,

$$\left.\frac{df}{dx}\right|_{x_m} = \frac{\frac{1}{2}f_{m-2} - 2f_{m-1} + \frac{3}{2}f_m}{\Delta x} \tag{65}$$

$$\left.\frac{d^2f}{dx^2}\right|_{x_m} = \frac{-f_{m-3} + 4f_{m-2} - 5f_{m-1} + 2f_m}{(\Delta x)^2} \tag{66}$$

$$\left.\frac{d^3f}{dx^3}\right|_{x_m} = \frac{\frac{3}{2}f_{m-4} - 7f_{m-3} + 12f_{m-2} + 9f_{m-1} + \frac{5}{2}f_m}{(\Delta x)^3} \tag{67}$$

$$\left.\frac{d^4f}{dx^4}\right|_{x_m} = \frac{-2f_{m-5} + 11f_{m-4} - 24f_{m-3} + 26f_{m-2} - 14f_{m-1} + 3f_m}{(\Delta x)^4}. \tag{68}$$

While the principles are simple, implementing boundary conditions requires tedious book-keeping. Accordingly, we illustrate one example where we apply the boundary conditions

$$\phi_p(x=0) = \phi_p^{\mathrm{b}} \qquad \left.\frac{d\phi_p}{dx}\right|_{x=0} = 0 \tag{69}$$

$$\phi_n(x=0) = \phi_n^{\mathrm{b}} \qquad \left.\frac{d\phi_n}{dx}\right|_{x=0} = 0 \tag{70}$$

to the diffusion equation, Eq. 16. We do not show an example using the momentum equation, but the procedure is identical. The first block row of $\boldsymbol{A}_{ij}\phi_j = \boldsymbol{b}_i$ contains the first boundary condition and is given by

$$\begin{bmatrix} 1 & 0 & \dots \\ 0 & 1 & \dots \end{bmatrix} \begin{bmatrix} \phi_{p,0} \\ \phi_{n,0} \\ \vdots \end{bmatrix} = \begin{bmatrix} \phi_p^{\mathrm{b}} \\ \phi_n^{\mathrm{b}} \end{bmatrix}. \tag{71}$$

The second boundary condition is given on the second block row,

$$\begin{bmatrix} -\frac{3}{2} & 0 & 2 & 0 & -\frac{1}{2} & 0 & \dots \\ 0 & -\frac{3}{2} & 0 & 2 & 0 & -\frac{1}{2} & \dots \end{bmatrix} \begin{bmatrix} \phi_{p,0} \\ \phi_{n,0} \\ \phi_{p,1} \\ \phi_{n,1} \\ \phi_{p,2} \\ \phi_{n,2} \\ \vdots \end{bmatrix} = \begin{bmatrix} 0 \\ 0 \end{bmatrix}. \tag{72}$$

Note that applying these boundary conditions requires altering both the right and left hand side of Eq. 16.

Non-periodic cases of Eq. 16 and Eq. 32 can be solved using a block-banded matrix solver. However, when using periodic boundary conditions with the hybrid FD/PS method, both matrices become cyclic. In this situation, we use the Sherman-Morrison-Woodbury formula,[S7] which allows one to get rid of the off-diagonal block elements and recover an $\mathrm{O}(\mathcal{M})$ method.

Theory of Surface-Directed Spinodal Decomposition

Despite the fact that we do not have a direct solution of surface-directed spinodal decomposition for our ternary Flory-Huggins model, we can still be quantitative and use a prediction of the front velocity v^* and dominant wavenumber q^* that Ball and Essery obtain based solely on the dispersion relation of the linearized theory. Using the so-called marginal stability hypothesis,[S8–S10] they predict that the front velocity and dominant wave number are,

$$v^* \approx 4.588 M \kappa q_m^3 \tag{73}$$

$$q^* \approx 1.083 q_m \tag{74}$$

where q_m is the fastest growing mode from the linear stability analysis.

In a previous publication,[S1] we looked at perturbations about a homogeneous state inside the spinodal using the model described in Eq. 10 in the main text. Assuming a constant scalar mobility M and pseudo-binary parameters, the dynamics of the most unstable eigenmode of the system gives an identical dispersion relation to that obtained by Ball and Essery, which in our notation is expressed as the largest eigenvalue,

$$\lambda_+(q) = M\kappa q^2(2q_m^2 - q^2). \tag{75}$$

Because the dispersion relations are identical, Equations 73 and 74 remain valid for our system, where the fastest growing mode is given by

$$q_m^2 = \frac{1}{4\kappa}\left[-\left(\frac{1}{N\phi_p} + \frac{2}{\phi_s} + \frac{1}{\phi_n}\right) + \sqrt{\left(\frac{1}{N\phi_p} - \frac{1}{\phi_n}\right)^2 + 4\left(\frac{1}{\phi_s} + \chi\right)}\right]. \tag{76}$$

Compared to the previous theoretical results, the above analysis of surface directed spinodal decomposition assumes the initial condition is prepared in an unstable state. Diffusion from the bulk is present via a boundary condition, but it does not drive the phase separation. Additionally, the analysis is limited to early-time behavior; we cannot infer anything about coarsening processes that happen at late times.

Surface-directed spinodal decomposition also introduces new timescales. The timescale for propagation of the spinodal wave through the film is given by $l_\mathrm{f}/v^* \sim l_\mathrm{f}/(M\kappa q_m^3)$. However, if noise is present (even if only in the initial condition), the bulk of the film is expected to undergo isotropic spinodal decomposition away from the interface at a time $\lambda_+(q_m)^{-1} = 1/(M\kappa q_m^4)$. Combining this rate and the wave velocity gives a prediction of a length scale, $1/q_m$, at which a crossover should happen between surface-directed and bulk spinodal decomposition. While this length scale is the same as the dominant wavelength, the numerical prefactor will surely differ since the crossover length is sensitive to the strength of

the density fluctuations and properties of the interface.[S8]

Data Tables

As discussed in the methods section, the data contained in the paper is from multiple simulation data sets. For the early-time regime 1D, 2D and 3D simulations were performed with periodic boundary conditions for $t = \{0, 2, \ldots, 100\}\tau_R$ where τ_R is the Rouse time of the reference polymer.[S1] In 1D simulations the domain was large ($L_x = 4096R_0$) and the bath/film interface was set in the middle of the domain ($f = 0.5$). Recall that an initial condition which is symmetric about x must be used to satisfy the periodic boundary conditions, as in Figure 2, halving the usable domain size. By necessity, 2D and 3D simulations were run in smaller domains: $L_x = 512R_0$, $L_y = 256R_0$ for 2D and $L_x = 64R_0$, $L_y = 64R_0$, $L_z = 64R_0$ for 3D. In all cases, the plane wave resolution was $2 \times R_0$, i.e. $N_x = 2L_x$, etc.

For the late-time regime 1D simulations were also performed with periodic boundary conditions in a very long domain ($L_x = 4096R_0$) for times $t = \{0, 100, \ldots, 5000\}\tau_R$. Unlike the short-time calculations, the initial film thickness was varied for the longer time runs with $f = \{0.025, 0.05, 0.1\}$ where $l_f = fL_x/2$. 2D and 3D simulations were performed with a truncated bath where an accompanying 1D simulation served as both the initial condition and the time-dependent bath boundary condition. Again, 2D and 3D simulations were run in smaller domains than were possible in 1D: $L_x = 128R_0$, $L_y = 128R_0$ for 2D and $L_x = 128R_0$, $L_y = 64R_0$, $L_z = 32R_0$ for 3D. For the 2D and 3D simulations with proscribed boundary conditions, the resolution was increased to $4 \times R_0$ to account for the lower accuracy of finite difference formulas relative to pseudospectral derivatives.

Below, we give three tables which summarize specific parameters where the data was taken. Table S1 gives the free energy model (ternary Flory-Huggins) parameters which were used. We have tried to be explicit in the main text, but unless otherwise noted, data were taken using the "Base Case" given in the first line of the table. The remaining two tables show

the initial film concentrations used in various simulations; Table S2 shows a coarse sweep of composition space and Table S3 shows a finer sweep. All of the initial film compositions used in the main text come from one of these two tables (e.g. Figure 5, Figure 7, and Figure 9). To aid the reader, Figure S1 shows both of these sets of initial conditions plotted in composition space with their corresponding run number.

Table S1: Energy model parameters used in all simulations. In all cases $\kappa_{pn} = \kappa_{ps}$, $\chi_{ps} = 0$ and $N_s = N_n = 1$.

ID	N_p	χ_{pn}	χ_{ns}	κ
"Base case"	20	1.04805	0	2
"N=10"	10	1.21272	0	3.36866
"N=50"	50	0.91199	0	12.66652
"$\chi_{pn} = 1.2\chi_c$"	20	0.89833	0	2.49536
"$\chi_{pn} = 1.6\chi_c$"	20	1.19777	0	9.98142
"$\chi_{ns} = 0.6\chi_c$"	20	1.04805	0.6	5.82250
"$\chi_{ns} = 1.2\chi_c$"	20	1.04805	1.2	5.82250

Table S2: Coarse resolution sweep of the volume fraction of the film initial condition. The initial bath concentration was always set to: $\phi_p = 0.01$, $\phi_n = 0.98$ and $\phi_s = 0.01$.

Run no.	ϕ_p	ϕ_n	ϕ_s	Run no.	ϕ_p	ϕ_n	ϕ_s
0	0.010	0.010	0.980	33	0.301	0.301	0.398
1	0.010	0.107	0.883	34	0.301	0.398	0.301
2	0.010	0.204	0.786	35	0.301	0.495	0.204
3	0.010	0.301	0.689	36	0.301	0.592	0.107
4	0.010	0.398	0.592	37	0.301	0.689	0.010
5	0.010	0.495	0.495	38	0.398	0.010	0.592
6	0.010	0.592	0.398	39	0.398	0.107	0.495
7	0.010	0.689	0.301	40	0.398	0.204	0.398
8	0.010	0.786	0.204	41	0.398	0.301	0.301

9	0.010	0.883	0.107	42	0.398	0.398	0.204
10	0.010	0.980	0.010	43	0.398	0.495	0.107
11	0.107	0.010	0.883	44	0.398	0.592	0.010
12	0.107	0.107	0.786	45	0.495	0.010	0.495
13	0.107	0.204	0.689	46	0.495	0.107	0.398
14	0.107	0.301	0.592	47	0.495	0.204	0.301
15	0.107	0.398	0.495	48	0.495	0.301	0.204
16	0.107	0.495	0.398	49	0.495	0.398	0.107
17	0.107	0.592	0.301	50	0.495	0.495	0.010
18	0.107	0.689	0.204	51	0.592	0.010	0.398
19	0.107	0.786	0.107	52	0.592	0.107	0.301
20	0.107	0.883	0.010	53	0.592	0.204	0.204
21	0.204	0.010	0.786	54	0.592	0.301	0.107
22	0.204	0.107	0.689	55	0.592	0.398	0.010
23	0.204	0.204	0.592	56	0.689	0.010	0.301
24	0.204	0.301	0.495	57	0.689	0.107	0.204
25	0.204	0.398	0.398	58	0.689	0.204	0.107
26	0.204	0.495	0.301	59	0.689	0.301	0.010
27	0.204	0.592	0.204	60	0.786	0.010	0.204
28	0.204	0.689	0.107	61	0.786	0.107	0.107
29	0.204	0.786	0.010	62	0.786	0.204	0.010
30	0.301	0.010	0.689	63	0.883	0.010	0.107
31	0.301	0.107	0.592	64	0.883	0.107	0.010
32	0.301	0.204	0.495	65	0.980	0.010	0.010

Table S3: Fine resolution sweep of the initial volume fraction of the film. The initial bath concentration was always set to: $\phi_p = 0.01$, $\phi_n = 0.98$ and $\phi_s = 0.01$.

Run no.	ϕ_p	ϕ_n	ϕ_s	Run no.	ϕ_p	ϕ_n	ϕ_s
0	0.010	0.010	0.980	116	0.301	0.253	0.446
1	0.010	0.059	0.931	117	0.301	0.301	0.398
2	0.010	0.107	0.883	118	0.301	0.350	0.349
3	0.010	0.156	0.835	119	0.301	0.398	0.301
4	0.010	0.204	0.786	120	0.301	0.447	0.252
5	0.010	0.253	0.738	121	0.301	0.495	0.204
6	0.010	0.301	0.689	122	0.301	0.543	0.155
7	0.010	0.350	0.640	123	0.301	0.592	0.107
8	0.010	0.398	0.592	124	0.301	0.641	0.058
9	0.010	0.447	0.543	125	0.301	0.689	0.010
10	0.010	0.495	0.495	126	0.350	0.010	0.640
11	0.010	0.543	0.447	127	0.350	0.059	0.592
12	0.010	0.592	0.398	128	0.350	0.107	0.543
13	0.010	0.641	0.349	129	0.350	0.156	0.495
14	0.010	0.689	0.301	130	0.350	0.204	0.446
15	0.010	0.738	0.252	131	0.350	0.253	0.398
16	0.010	0.786	0.204	132	0.350	0.301	0.349
17	0.010	0.835	0.155	133	0.350	0.350	0.301
18	0.010	0.883	0.107	134	0.350	0.398	0.252
19	0.010	0.931	0.058	135	0.350	0.447	0.204
20	0.010	0.980	0.010	136	0.350	0.495	0.155
21	0.059	0.010	0.931	137	0.350	0.543	0.107
22	0.059	0.059	0.883	138	0.350	0.592	0.058
23	0.059	0.107	0.835	139	0.350	0.641	0.010
24	0.059	0.156	0.786	140	0.398	0.010	0.592

25	0.059	0.204	0.738	141	0.398	0.059	0.543
26	0.059	0.253	0.689	142	0.398	0.107	0.495
27	0.059	0.301	0.640	143	0.398	0.156	0.446
28	0.059	0.350	0.592	144	0.398	0.204	0.398
29	0.059	0.398	0.543	145	0.398	0.253	0.349
30	0.059	0.447	0.495	146	0.398	0.301	0.301
31	0.059	0.495	0.447	147	0.398	0.350	0.252
32	0.059	0.543	0.398	148	0.398	0.398	0.204
33	0.059	0.592	0.349	149	0.398	0.447	0.155
34	0.059	0.641	0.301	150	0.398	0.495	0.107
35	0.059	0.689	0.252	151	0.398	0.543	0.058
36	0.059	0.738	0.204	152	0.398	0.592	0.010
37	0.059	0.786	0.155	153	0.447	0.010	0.543
38	0.059	0.835	0.107	154	0.447	0.059	0.495
39	0.059	0.883	0.058	155	0.447	0.107	0.447
40	0.059	0.931	0.010	156	0.447	0.156	0.398
41	0.107	0.010	0.883	157	0.447	0.204	0.349
42	0.107	0.059	0.835	158	0.447	0.253	0.301
43	0.107	0.107	0.786	159	0.447	0.301	0.252
44	0.107	0.156	0.738	160	0.447	0.350	0.204
45	0.107	0.204	0.689	161	0.447	0.398	0.155
46	0.107	0.253	0.641	162	0.447	0.447	0.107
47	0.107	0.301	0.592	163	0.447	0.495	0.058
48	0.107	0.350	0.543	164	0.447	0.543	0.010
49	0.107	0.398	0.495	165	0.495	0.010	0.495
50	0.107	0.447	0.447	166	0.495	0.059	0.447
51	0.107	0.495	0.398	167	0.495	0.107	0.398

52	0.107	0.543	0.350	168	0.495	0.156	0.349
53	0.107	0.592	0.301	169	0.495	0.204	0.301
54	0.107	0.641	0.252	170	0.495	0.253	0.253
55	0.107	0.689	0.204	171	0.495	0.301	0.204
56	0.107	0.738	0.155	172	0.495	0.350	0.155
57	0.107	0.786	0.107	173	0.495	0.398	0.107
58	0.107	0.835	0.058	174	0.495	0.447	0.058
59	0.107	0.883	0.010	175	0.495	0.495	0.010
60	0.156	0.010	0.835	176	0.543	0.010	0.447
61	0.156	0.059	0.786	177	0.543	0.059	0.398
62	0.156	0.107	0.738	178	0.543	0.107	0.350
63	0.156	0.156	0.689	179	0.543	0.156	0.301
64	0.156	0.204	0.641	180	0.543	0.204	0.253
65	0.156	0.253	0.592	181	0.543	0.253	0.204
66	0.156	0.301	0.543	182	0.543	0.301	0.155
67	0.156	0.350	0.495	183	0.543	0.350	0.107
68	0.156	0.398	0.447	184	0.543	0.398	0.058
69	0.156	0.447	0.398	185	0.543	0.447	0.010
70	0.156	0.495	0.350	186	0.592	0.010	0.398
71	0.156	0.543	0.301	187	0.592	0.059	0.349
72	0.156	0.592	0.252	188	0.592	0.107	0.301
73	0.156	0.641	0.204	189	0.592	0.156	0.252
74	0.156	0.689	0.155	190	0.592	0.204	0.204
75	0.156	0.738	0.107	191	0.592	0.253	0.155
76	0.156	0.786	0.058	192	0.592	0.301	0.107
77	0.156	0.835	0.010	193	0.592	0.350	0.058
78	0.204	0.010	0.786	194	0.592	0.398	0.010

79	0.204	0.059	0.738	195	0.641	0.010	0.349
80	0.204	0.107	0.689	196	0.641	0.059	0.301
81	0.204	0.156	0.641	197	0.641	0.107	0.252
82	0.204	0.204	0.592	198	0.641	0.156	0.204
83	0.204	0.253	0.544	199	0.641	0.204	0.155
84	0.204	0.301	0.495	200	0.641	0.253	0.107
85	0.204	0.350	0.447	201	0.641	0.301	0.058
86	0.204	0.398	0.398	202	0.641	0.350	0.010
87	0.204	0.447	0.350	203	0.689	0.010	0.301
88	0.204	0.495	0.301	204	0.689	0.059	0.252
89	0.204	0.543	0.253	205	0.689	0.107	0.204
90	0.204	0.592	0.204	206	0.689	0.156	0.155
91	0.204	0.641	0.155	207	0.689	0.204	0.107
92	0.204	0.689	0.107	208	0.689	0.253	0.058
93	0.204	0.738	0.058	209	0.689	0.301	0.010
94	0.204	0.786	0.010	210	0.738	0.010	0.252
95	0.253	0.010	0.738	211	0.738	0.059	0.204
96	0.253	0.059	0.689	212	0.738	0.107	0.155
97	0.253	0.107	0.641	213	0.738	0.156	0.107
98	0.253	0.156	0.592	214	0.738	0.204	0.058
99	0.253	0.204	0.544	215	0.738	0.253	0.010
100	0.253	0.253	0.495	216	0.786	0.010	0.204
101	0.253	0.301	0.447	217	0.786	0.059	0.155
102	0.253	0.350	0.398	218	0.786	0.107	0.107
103	0.253	0.398	0.350	219	0.786	0.156	0.058
104	0.253	0.447	0.301	220	0.786	0.204	0.010
105	0.253	0.495	0.253	221	0.835	0.010	0.155

106	0.253	0.543	0.204	222	0.835	0.059	0.107
107	0.253	0.592	0.155	223	0.835	0.107	0.058
108	0.253	0.641	0.107	224	0.835	0.156	0.010
109	0.253	0.689	0.058	225	0.883	0.010	0.107
110	0.253	0.738	0.010	226	0.883	0.059	0.058
111	0.301	0.010	0.689	227	0.883	0.107	0.010
112	0.301	0.059	0.640	228	0.931	0.010	0.059
113	0.301	0.107	0.592	229	0.931	0.059	0.010
114	0.301	0.156	0.543	230	0.980	0.010	0.010
115	0.301	0.204	0.495				

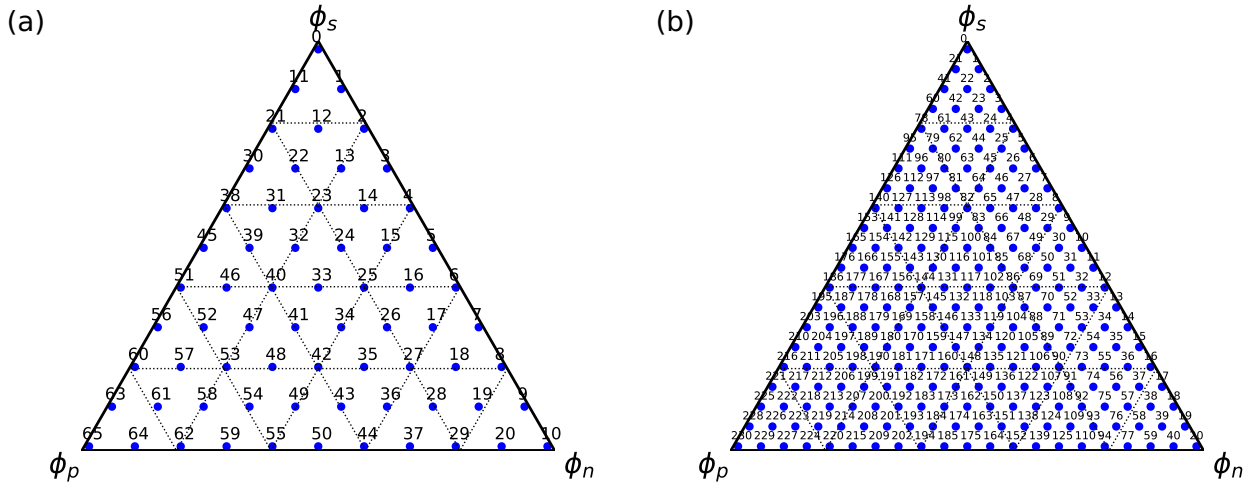

Figure S1: (a) A coarse sweep and (b) a fine sweep of the composition of the film initial condition.

Parameter Studies of the Early-Time Regimes

One can gain additional insight into the kinetic regimes by examining the effects of model parameters. Accordingly, Figure S2 categorizes the early-time kinetic regimes of several different data sets by their initial condition by systematically varying N_p, χ_{pn} and χ_{ns}. Note

that these parameters affect both the phase diagram as well as kinetics parameters, such as the mutual diffusion coefficient.[S1] We will briefly examine the effect of each parameter in turn.

Figure S2(a), S2(c) and S2(d) show results from three data sets where the solvent/nonsolvent interaction parameter, χ_{ns}, varies from 0 to 1.2, at constant N_p and χ_{np}. The phase diagram in these cases shifts only slightly, and one observes little change in the location of regimes I and II with changing χ_{ns}. These observations agree with our earlier conclusion that the local concentration of the interface plays a dominant role in distinguishing between regimes I and II/III. By contrast, regime III is quite sensitive to the change in the interaction parameter, and shrinks considerably as χ_{ns} increases. We hypothesize that a change in the rate of solvent/nonsolvent exchange is the primary cause. Increasing χ_{ns} decreases the nonsolvent diffusion relative to polymer diffusion and leads to a smaller "tail" on the film side of the composition path, which in turn gives a smaller region for regime III.

Figure S2(b), S2(d) and S2(e) show data sets where the polymer degree of polymerization, N_p, varies from 10 to 50, $\chi_{ns} = 0$ and χ_{np} is held at a constant ratio to its binary critical value. In this case, the phase diagram narrows, and shifts towards smaller polymer concentrations as N_p increases. The change in the boundary between regime I and regimes II/III is again modest, with a small increase in the region of the composition space taken by II and III as N_p increases. The most notable difference however, is the shift of regime III to the right, which mirrors the movement of the spinodal region as the phase diagram shifts. This shift is again consistent with our observation that the tail of the composition path due to the polymer film must cross into the spinodal for regime III to occur.

Figure S2(d), S2(f) and S2(g) show data where N_p and χ_{ns} are held constant, while χ_{np} varies from $1.2\chi_c$ to $1.6\chi_c$ where

$$\chi_c = \frac{1}{2}\left(\frac{1}{N_n^{1/2}} + \frac{1}{N_p^{1/2}}\right)^2 \tag{77}$$

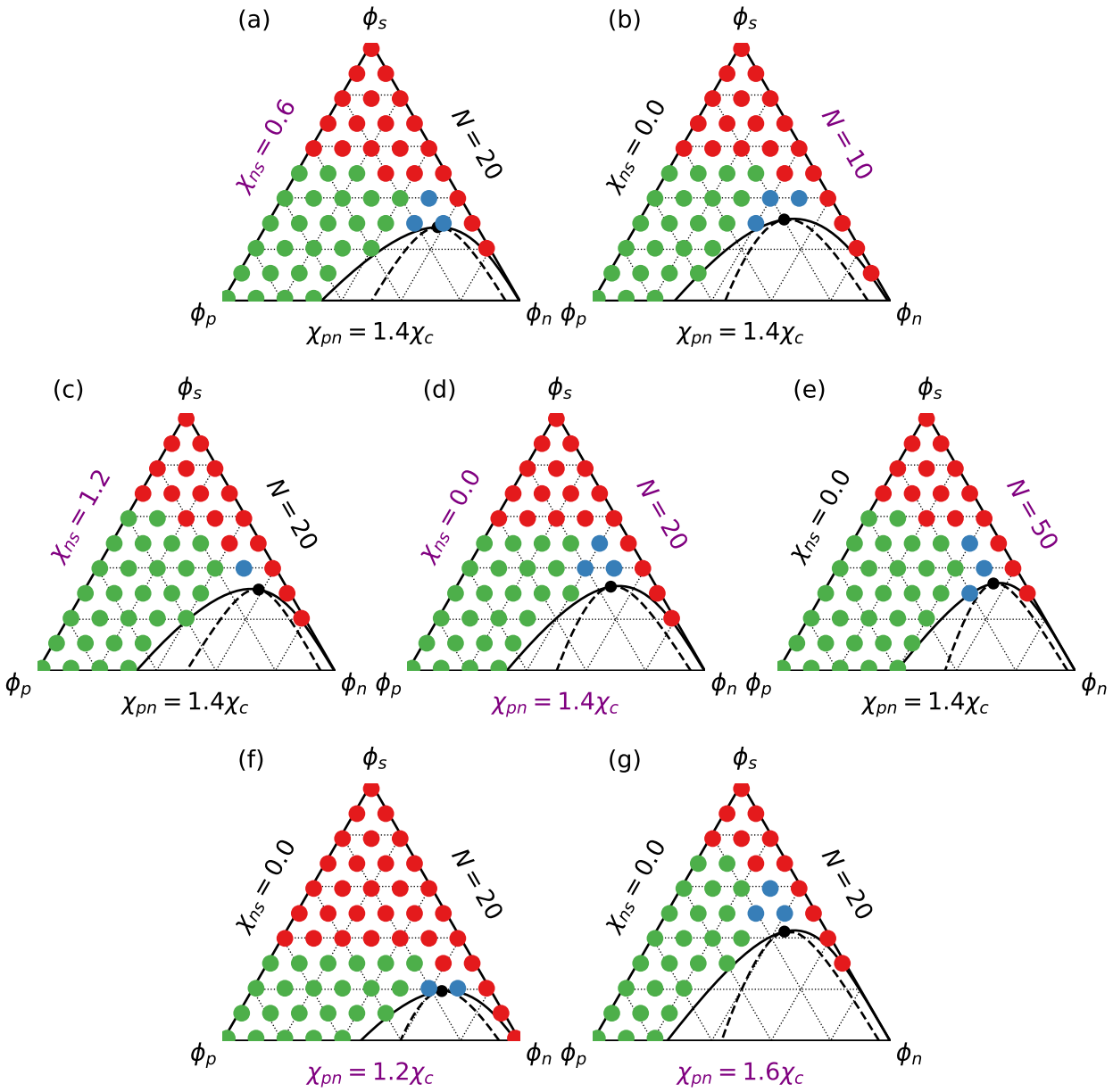

Figure S2: Characterization of the early-time kinetic regime by initial condition for the seven different sets of parameters labeled in the figure. Note that: panel (d) is the base case, χ_{ns} varies in the upper left panels (a, c, d), N_p varies in the upper right panels (b, d, e) and χ_{pn} varies in the bottom panels (d, f, g). Conditions which lead to regime I (no phase separation) appear as red dots, regime II (phase separation) appear as green dots and regime III (immediate spinodal decomposition) appear as blue dots.

is the critical Flory Huggins parameter for a binary mixture of polymer and nonsolvent. As χ_{np} increases, the quench deepens and the two-phase region expands to cover a larger amount of the composition space. Concomitantly, the size of regimes II and III also increase, and by $\chi_{np} = 1.6\chi_c$, there is only a small region of regime I remaining.

Time Invariance When Films Precipitate

In the main text, we claim that at late times, the system dynamics can be characterized by two dimensionless numbers, ξ and tD_0/l_f^2. We use Figure 8 as evidence for this claim, since both real space and composition space curves collapse when scaled appropriately. Figure S3 provides further evidence, showing a similar calculation (parameters $N_p = 20$, $\chi_{pn} = 1.048$, $\kappa = 2$) chosen at a different initial condition: $\{\phi_p^{\mathrm{f}}, \phi_n^{\mathrm{f}}\} = \{0.204, 0.301\}$ and $\{\phi_p^{\mathrm{b}}, \phi_n^{\mathrm{b}}\} = \{0.01, 0.98\}$.

Unlike the figure in the main text, at this initial condition, the system undergoes spinodal decomposition at long times (i.e. late time regime III). Even so, one still observes from the figure that when the length and time are appropriately scaled, the diffusive transport remains identical. Notably, in the inset in Figure S3(b) there is not an exact correspondance in the domain location following surface directed spinodal decompostion. This is to be expected since the phase separation kinetics add additional time and length scales, and are also dependent on the stochastic nature of the initial condition.

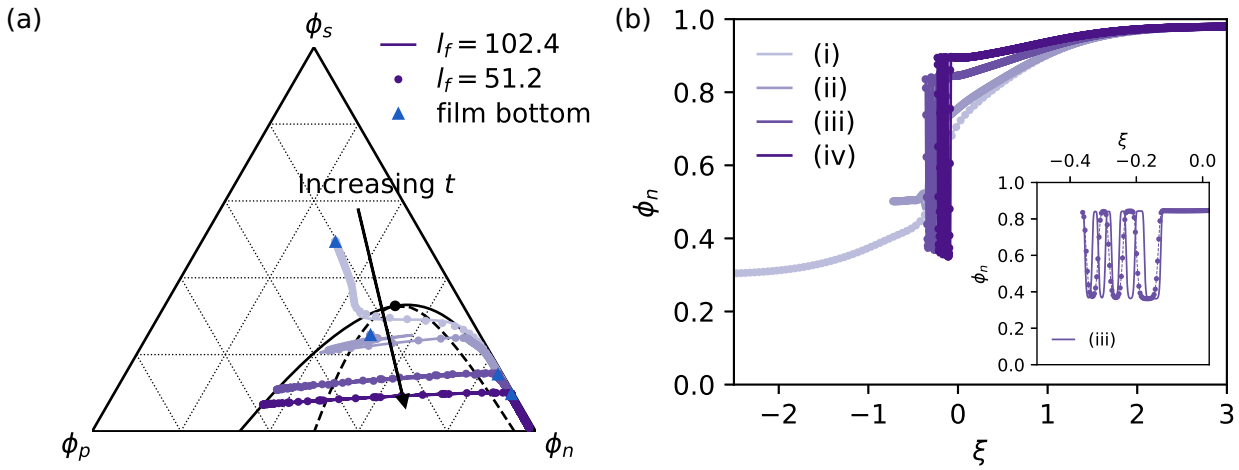

Figure S3: Comparison of the long time diffusion dynamics between two differnet film thicknesses in (a) composition space and (b) real space. The solid curves show a film thickess of $l_\mathrm{f} = 102.4$ at time points (i) 10, (ii) 500, (iii) 2×10^3, and (iv) 5×10^3 (in units of the Rouse time). The closed circles show a film thickness of $l_\mathrm{f} = 51.2$ at time points (i) 2.5, (ii) 125, (iii) 500, and (iv) 1.25×10^3 The inset depicts a zoomed-in portion of the real space volume fraction profile curve (iii).

References

(S1) Tree, D. R.; Delaney, K. T.; Ceniceros, H. D.; Iwama, T.; Fredrickson, G. H. A multi-fluid model for microstructure formation in polymer membranes. *Soft Matter* **2017**, *13*, 3013–3030, DOI: 10.1039/C6SM02839J.

(S2) Hur, S.-M.; Garcia-Cervera, C. J.; Fredrickson, G. H. Chebyshev Collocation in Polymer Field Theory: Application to Wetting Phenomena. *Macromolecules* **2012**, *45*, 2905–2919, DOI: 10.1021/ma202427n.

(S3) Fredrickson, G. H. *The Equilibrium Theory of Inhomogeneous Polymers*; Oxford University Press, 2006.

(S4) Fornberg, B. Generation of finite difference formulas on arbitrarily spaced grids. *Math. Comp.* **1988**, *51*, 699–699, DOI: 10.1090/s0025-5718-1988-0935077-0.

(S5) Ford Versypt, A. N.; Braatz, R. D. Analysis of finite difference discretization schemes for diffusion in spheres with variable diffusivity. *Comput. Chem. Eng.* **2014**, *71*, 241–252, DOI: 10.1016/j.compchemeng.2014.05.022.

(S6) Rempfer, D. On Boundary Conditions for Incompressible Navier-Stokes Problems. *Appl. Mech. Rev.* **2006**, *59*, 107, DOI: 10.1115/1.2177683.

(S7) Press, W. H.; Teukolsky, S. A.; Vetterling, W. T.; Flannery, B. P. *Numerical Recipes in C++: The Art of Scientific Computing, 2nd Edition*; Cambridge University Press, 2002.

(S8) Ball, R. C.; Essery, R. L. H. Spinodal decomposition and pattern formation near surfaces. *J. Phys.: Condens. Matter* **1990**, *2*, 10303–10320, DOI: 10.1088/0953-8984/2/51/006.

(S9) van Saarloos, W. Dynamical velocity selection: Marginal stability. *Phys. Rev. Lett.* **1987**, *58*, 2571–2574, DOI: 10.1103/physrevlett.58.2571.

(S10) van Saarloos, W. Front propagation into unstable states: Marginal stability as a dynamical mechanism for velocity selection. *Phys. Rev. A* **1988**, *37*, 211–229, DOI: 10.1103/physreva.37.211.